Nano Research
2024, 17(3): 1151–1164

ISSN 1998-0124 CN 11-5974/O4
https://doi.org/10.1007/s12274-023-5943-0

Research Article

Applying heteroatom co-doped carbon nanotube for manifesting high performance in the electrochemical reduction of aqueous nitrogen oxide by gold nanoparticles

Jane Chung[1,2,§], Haibo Yin[1,§], Rong Wang[1], Yunlong Wang[1], Junyang Zhang[1], Yue Peng[1], Joung Woo Han[2], Seongyun Ryu[2], and Junhua Li[1] (✉)

[1] State Key Joint Laboratory of Environment Simulation and Pollution Control, School of Environment, Tsinghua University, Beijing 100084, China
[2] EHS Research Center, Samsung Electronics Co., Ltd., Gyeonggi-do 18448, Republic of Korea
[§] Jane Chung and Haibo Yin contributed equally to this work.

Received: 4 May 2023 / **Revised:** 19 June 2023 / **Accepted:** 20 June 2023

ABSTRACT

Electrochemical NO-to-NH_3 under ambient conditions could be a viable alternative having advantages in terms of energy consumption and exhaust gas recycling of NO, replacing a traditional ammonia synthesis method of the Haber–Bosch process. In synthesizing boron (B-) and nitrogen (N-) co-doped carbon nanotube (CNT) based gold (Au) catalysts, B-dopants elevate the conductivity of carbon nanotube by sp^2 hybridization on graphene and implant B–N domains within the graphene layer, and result in facilitating the embedding amount of Au accompanied by high dispersibility with low particle size. Theoretical density functional theory (DFT) calculations elucidate that the electron cloud transmitted from B-dopant to the active site of Au induces the Lewis acidic site, and the O-distal pathway occurs following a spontaneous reaction. Increment of the electron-deficient B-doping area accompanied by N-defects and B–O edges retains the major valence state of Au as $Au^{\delta+}$, and suppresses hydrogen evolution reaction (HER) by repulsing the hindrance of H*. This record exhibits the highest faradaic efficiency (FE) of 94.7%, and NH_3 yield rate of 1877.4 $\mu g \cdot h^{-1} \cdot mg_{cat}^{-1}$, which is the optimal yield over energy consumption in the field of the ambient reduction of aqueous NO.

KEYWORDS

boron heteroatom, nitrogen defect, gold nanoparticles, valence states of gold, electrochemical NO-to-NH_3

1 Introduction

Nitrogen oxide (NO_x) is an unavoidable hazardous gas prevalently emitted from the fossil fuel burner of industrial devices and diesel engines in vehicles, being cited as a direct candidate resulting in serious harm to human respiratory and optic organs, as well as environments such as acid rain, photochemical heavy smog, and global warming [1, 2]. Anthropogenic NO_x emissions cause and accelerate imbalances in the natural nitrogen cycle, necessitating innovative approaches to reduce NO_x emissions, especially for major sources of emission from power plants, manufacturing factories, and automobiles [3, 4].

To prevent excessive NO_x emissions, typical post-combustion methods such as high-temperature treatment and selective adsorption–desorption have been flexibly applied in industrial and automotive settings. Thermal treatment is classified by the presence of catalysts, which are selective catalytic reduction (SCR) and selective non-catalytic reduction (SNCR) [5, 6]. Today, these thermal treatment methods have already achieved one-hundred percent converting efficiency in converting NO_x to a harmless form of N_2 but still have issues to address related to the hazardous in processing under high temperature (SCR > 150 °C and SNCR > 800 °C) and the requirement of the considerable amount of the extra reducing agents (e.g. urea and ammonia (NH_3)) [5, 7].

Moreover, recycling NO_x as a valuable N-source beyond converting to a harmless product has been actively studied as a remarkable approach, especially among candidates. NH_3 is considered a profitable material as a fertilizer, an essential substrate for the manufacturing industry, and a hydrogen energy carrier with a high-power density (4.3 $kWh \cdot kg^{-1}$) [8, 9]. Although the Haber–Bosch process is a traditional century-old method for producing NH_3 from nitrogen (N_2-to-NH_3) successfully [10, 11], it demands harsh temperature and pressure for dissociating N_2 into single N (941 $kJ \cdot mol^{-1}$) and the necessary of hydrogen source from the combustion of fossil fuel [12, 13]. Thus, the electrochemical method, which is able to operate under ambient conditions and convert renewable electrical energy into a chemical substrate directly, has been considered a new paradigm [14–18]. Furthermore, a promising approach to synthesizing NH_3 using NO_x, known as electrochemical NO_x reduction reaction (eNO_xRR), has emerged to overcome the limitation of low productivity of N_2 (~ 5×10^{-6} $mol \cdot cm^{-2} \cdot h^{-1}$) that does not reach the US department of energy (DOE) target (3.4×10^{-3} $mol \cdot cm^{-2} \cdot h^{-1}$) [19–21], and for requiring less electron consumption than nitrate (8 electrons per nitrate) [22]. Theoretical calculations suggest that the conversion of NO_x to NH_3 requires fewer electrons, as demonstrated by the following equation: $NO(g) + 6H^+ + 5e^- \rightarrow$

Address correspondence to lijunhua@tsinghua.edu.cn

$NH_4^+ + H_2O$ (E^0 = 0.836 V_{NHE}) [23]. The faradaic efficiency (FE) and yields for NH_3 synthesis under aqueous and gaseous NO_x were respectively reported as 77% of FE and 8398 $\mu g \cdot h^{-1} \cdot mg_{cat}^{-1}$ of yield with aqueous NO_x, and 96% of FE and 1239 $\mu mol\ cm^{-2} \cdot h^{-1}$ with gaseous NO_x [21, 23, 24]. As a result, ongoing research in electrochemical NO_x-to-NH_3 aims to develop a high-efficiency and low-energy consumption process. Moreover, the inherent advantages of scale-up flexibility in electrical systems are expected to be applied directly to the various facilities that emit high concentrations of NO_x, such as transportation and semiconductor/display manufacturing, thus it is possible to evolve into an immediate recyclable technology at the emitting point (Fig. S1 in the Electronic Supplementary Material (ESM)).

Researchers have investigated different reaction pathways for NO_x-to-NH_3 depending on the types of catalytic metals (e.g. Fe, Cu, Pd, Pt, Co, Os, Ru, Au, and Nb), heteroatomic supports (e.g. boron nitride (BN), and binary heteroatom doped carbon), and carbon supports (e.g. C_2N, C_3N_4, graphene, and carbon nanotube (CNT)) [6, 21, 23–34]. Each catalyst that follows a distal or alternative mechanism has a different rate-limiting step (RDS). For instance, a step resulting in HNO_{ads} by the first hydrogenation on niobium carbon nanotube [21] or a step in forming H_2NO on the metal catalyst surface of Fe(110) and Pt(100) [23, 28] required the highest activation energy. Thus, in the view of addressing demands related to the activation energy, researchers are striving to innovate the structure and configuration of metal and non-metal catalysts, transform the phase of NO_x to gas or aquatic condition, add the selective absorbent and organic frameworks for NO_x fixation, and even combine with the external assistant energy (e.g. plasma) to overcome the biggest energetic hurdle of RDS [23, 25, 26, 35–38].

Heteroatomic carbon supports containing binary atoms (B, N, P, and S) enhance stability in anchoring metallic catalyst on carbon support as a single unit with high dispersibility, and promote electrochemical efficiency by facilitating conductivity and catalytic activity [34, 38–43]. The different electronegativities of heteroatoms (B < C < N; 2.04 < 2.55 < 3.04) allow for tuning the band gap by changing the chemical composition, thus producing noteworthy activation in reduction reactions [45–47]. They also initiate breaking electroneutrality of carbon to promote the electrical capacity of carbon support and create more active sites [48–50]. In particular, boron can induce electron deficiencies within graphene, facilitating the chemisorption of negatively polarized reactants and repulsing Lewis acidic H^+ to suppress unwanted competing reactions [51–53]. Co-doping two or more heteroatoms have been studied recently; B and N co-doped carbon exhibited extraordinarily enlarged properties in morphology, porosity, surface oxygen functional groups, and electronic structure [48, 54–56]. Even the wettability of the interface between aqueous electrolytes and a solid electrode was improved [57].

Gold (Au) is a particular metallic catalyst that possesses high inherent conductivity and catalytic activity as well [58]. Additionally, it is capable of forming strong sp^2 carbon lattice bonds with heteroatom [59]. Due to these characteristics, Au has been investigated as a strong candidate for N_2-to-NH_3, and in fact, embedded Au is identified to be a crucial catalyst, creating stable Au-NH* intermediates throughout the reaction mechanism [47, 60–63]. In predicting the eNO_xRR pathway through density functional theory (DFT) calculation, since the same intermediate as above appears and the protonation reaction of NOH* is deemed as RDS, those desired reactions can be activated by Au in the same manner [64–66]. Recent studies have actively explored the use of new designs of Au catalyst to improve the efficiency of electrochemical reduction [66–68], however, in some cases, unexpected by-products of N–N dimers such as N_2O and N_2 have been observed, that to be interpreted as a reaction between adjacent N_{ads} adsorbates on the catalyst active site [69]. To mitigate the production of such by-products, researchers have attempted to reduce their likelihood by embedding metal catalysts as single atoms (SAs) [32, 70, 71], but interestingly, under some specific reduction reactions with SAs, catalytic activity has been rather reduced [27, 72]. Au, in particular, is challenging to embed as SAs since it readily aggregates into nanoparticles [42, 70], and can even exist in a form where nanoparticles and SA co-exist [73]. Besides, even if Au is doped as the nanoparticles, the charge of Au may differ depending on the metal anchoring atoms, potentially affecting the catalyst's activity [74], so research purposes on improving the dispersibility of Au and reducing its size through the appropriate combination of Au and heteroatoms is necessary.

These metallic carbon catalyst composites where exposed to the ambient atmosphere are enable the catalytic application, but conversely, the thicker carbon layer may hinder the desired access of mass transport due to its low porosity [38, 75]. To overcome this limitation, other types of carbon dimensions can be constructed by manipulating the molecular weight of the structural polymer of polyethylene glycol (PEG). Specifically, when PEG is applied as electrochemical catalyst support [21, 44, 45, 48], tuning the atomic bonds and achieving sufficient conductivity can be secured to properly support the metal catalyst and ensure a reaction part [41, 43]. In this regard, for elevating the stability of the catalyst, placing the actual reaction site of metallic catalyst and organic framework into the nanotube-type conductive carbon structure has also been studied as a practical strategy in the actual electrolysis [21, 38]. Furthermore, constructing a three-dimensional (3D) structure has been suggested for improving ion diffusivity and deriving homogeneously interconnected carbon nanotubes beyond the one-dimensional (1D) structure of carbon nanotube; herein, the macro-scaled conductive material of melamine foam (MF) has exhibited superior carbonaceous structure promoting higher pore volume and surface area [48, 76–78]. Its macro-scaled 3D structures have shown remarkable improvement, especially in the reaction of the gaseous reactant with high selectivity by mesoporous structure [56, 79, 80]. The application of the entangling tubular carbon nanotube on 3D MF structure has advanced the energy capacitance of catalytic electrodes in the area of energy storage [38, 48], achieving selectivity of NH_3 synthesis in actual NO_x-to-NH_3 reaching 77.0% [21]. In this perspective, our study purposes improving the electrical NH_3 synthesis efficiency by entangling Au-contained B and N co-doped carbon nanotube (noted as Au-BNC) on MF, thus the results showed an improvement in NO adsorption on the catalyst and exhibited 94.7% of high NH_3 selectivity in NO_x-to-NH_3 with stability for 12 h.

2 Experimental

2.1 Chemicals and materials

Polyethylene glycol (PEG-2000), urea (NH_2CONH_2), boric acid (H_3BO_3), chloroauric acid trihydrate ($HAuCl_4 \cdot 3H_2O$), dipotassium hydrogen phosphate (K_2HPO_4), potassium dihydrogen phosphate (KH_2PO_4), trichloroacetic acid solution ($C_2HCl_3O_2$), 8-quinolinol (C_9H_7NO), sodium carbonate anhydrous (Na_2CO_3), hydroxylamine solution (NH_2OH), potassium sodium tartrate tetrahydrate ($C_4H_4O_6KNa \cdot 4H_2O$), Nessler reagent (K_2HgI_4), sodium nitrite-^{15}N ($Na^{15}NO_2$), ammonium chloride-^{15}N ($^{15}NH_4Cl$), and maleic acid ($C_4H_4O_4$) were purchased from Shanghai Macklin Co., Ltd (China). Melamine foam ($C_3H_6N_6$) was purchased in commercial type. Hydrochloric acid (HCl), sulfuric acid (H_2SO_4),

and ammonium chloride (NH_4Cl) were purchased from Beijing Chemical Works (China), and ethanol (CH_3CH_2OH) and Deuterium oxide (D_2O) were purchased from Shanghai Aladdin Bio-Chem Technology Co., Ltd (China). 5% Nafion® 117 solution was purchased from Sigma-Aldrich. Nafion 117 membrane and carbon paper were purchased from GaossUnion (China), and the reaction gases of argon (Ar, > 99.999%) and NO (99.9%) were purchased from Beijing huatong jingke gas co., Ltd (China). All chemicals were used by analytic grades and deionized water (DIW) was prepared by Milli-Q water (18.2 MΩ·cm).

2.2 Preparation of Au-BNC and Au-NC

Synthesis of B and N co-doped carbon nanotube denoted as BNC was prepared as follows: 0.5 g PEG-2000, 5 g urea and 0.15 g H_3BO_3 were dissolved in 50 mL of DIW, and the homogeneous solution was obtained with stirring with 150 rpm for 30 min. 0.2 g of MF was immersed in the homogeneous mixture, and then, dried with heat in a vacuum oven at 80 °C for 24 h after thoroughly stirring at room temperature for 24 h. The pyrolysis was implemented consecutively in a fused-quartz tube heating at 900 °C for 6 h with the temperature increasing rate of 5 °C·min^{-1} under Ar atmosphere. The final calcined MF was ground by agate mortar and pestle, and the final BNC product was collected, after washing out with ethanol and DIW repeatedly for rinsing out the unreacted precursors and the foreign matter. The Au-embedded BNCs (Au-BNCs) were synthesized by manipulating the addition of 2 wt.% $HAuCl_4$ stock in the first step of preparing a homogeneous precursor mixture by the final Au concentration reaching 0.02, 0.05, 0.1, 0.2, 0.4, and 0.6 mM Au. For preparing the comparative group without the presence of B-dopant, Au-contained N doped graphene (Au-NC) was synthesized by getting rid of only boric acid in the homogeneous mixture.

2.3 Material characterization

The morphology of the prepared catalyst samples was observed by the field emission scanning electron microscopy (FESEM, ZEISS GEMINISEM 500 electron field emission microscope). Transmission electron microscopy (TEM, JEOL JEM-2100F) equipped with energy-dispersive spectroscopy (EDS) was performed with an accelerating voltage of 200 kV [81]. The sample was prepared by depositing catalyst suspension, which of dispersing the catalyst uniformly in ethanol with ultra-sonication, on a carbon-coated molybdenum mesh grid (Gilder 200 mesh, AG200M) and dried at room temperature [70]. High-angle annular dark-field scanning transmission electron microscopy (HAADF-STEM) images were obtained by using a Hitachi S-5500 with an accelerating voltage of 30 kV. X-ray diffraction (XRD) analyses were carried out using a BRUKER D8/Advance X-ray diffractometer with Cu Kα radiation source (λ = 1.5418 Å, 40 kV voltage, 40 mA current) at a scan rate of 10 °·min^{-1} within 2θ range of 10°–70°. Au contents incorporated in Au-BNC were analyzed by an inductively coupled plasma optical emission spectrometry (ICP-OES, Thermo Scientific IRIS Intrepid II). X-ray photoelectron spectroscopy (XPS) analysis was implemented using a Thermo Scientific ESCALAB 250XI photoelectron spectrometer with Al Kα X-ray radiation as the X-ray source (1486.7 eV) for excitation and the optimal energy resolution ≤ 0.45 eV. All binding energies were calibrated in reference to the C 1s main peak at 284.8 eV. Raman measurements were proceeded on a Confocal Raman microscope (Renishaw inVia) with laser excitation at 532 nm, and the spectral recording range was 500–4000 cm^{-1} [21]. Attenuated total reflectance infrared spectroscopy (ATR-IR) was recorded on a Thermo Fisher Scientific Nicolet IS 10 flourier transform IR spectrometer on KBr pellets. The nitrogen adsorption–desorption isotherms were implemented at −196 °C on MicrotracBEL Corp, and specific surface areas and pore size distribution were calculated according to multipoint Brunauer–Emmett–Teller (BET) and Barrett–Joyner–Halenda (BJH) [70, 81]. Prior to collecting data, the samples were degassed at 200 °C for 4 h under a vacuum [70]. Electron paramagnetic resonance (EPR) spectra were obtained with a JEOL FA-200 instrument at room temperature.

2.4 Installation of the electrochemical cell

The H-type electrolytic quartz cell was used for the electrochemical nitrogen oxide reduction reaction (NORR) test. Potentiostatic tests were performed using an electrochemical workstation (CHI760E, CH Instruments, Inc., Chenhua, Shanghai) equipped with a typical three-electrode system. Prepared catalyst carbon papers doping catalytic inks on the layer were applied to the working electrode (size: 1 cm × 0.5 cm), and an Ag/AgCl electrode (with saturated KCl as the filling solution) and the platinum plate (size: 1 cm × 1 cm) were respectively used for reference and counter electrodes. The cathode and anode compartments were separated by a proton exchange membrane (Nafion 117), which were softened by soaking in DIW overnight. 0.1 M HCl aqueous solution [21] was applied as an electrolyte and pre-purged with the relevant reaction gas for at least 30 min (10 sccm) in advance for proceeding with the electrochemical test in order to remove residual air in the electrolyte. 100 mL of the electrolyte solution was evenly distributed to the cathode and anode compartments, and the test was conducted under stirring at 100 rpm. As for reactant gas, NO gas (99.9%) was continuously injected with a flow rate of 20 sccm by a mass flow controller (MFC, D07–7, Beijing SevenStar Flow Co., Ltd). All of the measured potentials were converted to the reversible hydrogen electrode (RHE) using the Nernst equation potential as follows

$$E_{RHE}\,(V) = E_{Ag/AgCl}\,(V) + 0.0591 \times pH + E^{0}_{Ag/AgCl}$$

where E_{RHE} is the converted potential vs. RHE, $E^{0}_{Ag/AgCl}$ = 0.1976 V at 25 °C, and $E_{Ag/AgCl}$ is the experimentally measured potential vs. Ag/AgCl reference.

Linear sweep voltammetry (LSV) tests were conducted with NO and Ar saturated electrolyte along with the potential range from +0.7 to −1.3 V vs. RHE with a scan rate of 10 mV·s^{-1}. All LSV curves were induced under steady-state after repeating the prior cyclic operation several times and directly used without additional ohmic-drop correction [3, 70]. Cyclic voltammetry (CV) measurements were implemented with the potential windows from +1.7 to −1.3 V vs. RHE. For comparing real active surface sites on the working electrode, the electrochemical double layer capacitance (EDLC) was measured by scanning the CVs under each narrow potential window with different scan rates of 10, 20, 40, 60, 80, and 100 mV·s^{-1}. Every CVs were repeatedly scanned by swinging 10 cycles through the potential windows. Specific double layer capacitances (C_{dl}) were derived by plotting the charging current density difference ($\Delta j = (J_a - J_c)/2$) against the scan rates (v), where J_a and J_c respectively indicate anodic and cathodic current density. Electrochemical impedance spectroscopy (EIS) [82] measurements were conducted at the frequency range from 0.1 MHz to 10^{-2} Hz with an amplitude of 5 mV. All the above-mentioned measurements were conducted at room temperature under atmospheric pressure.

2.5 Product analysis

The electrochemical reduction reaction was conducted by means of chronoamperometry (CA) for 2 h, and the concentrations of the synthesized NH_3 and NH_2OH were measured by colorimetric methods. Dissolved ions by NH_3 to NH_4^+ and NH_2OH to NH_3OH^+ were detected by following their standard calibration

curves. Standard curves were displayed by preparing reference solutions with concentrations ranging from 0.4 to 4.0 ppm for NH_4^+ and 0.1 to 12.8 ppm for NH_3OH^+, and spectrophotometrically determined by ultraviolet-visible (UV–vis) spectrophotometer (DR6000, HACH Company Loveland, USA). The specific procedures are as follows:

Measurement of ammonia (NH_4^+)-N

The ionic concentrations of ammonia-N were determined using the colorimetric reagent of the Nessler reagent method [81]. A certain amount of electrolyte collected from the electrolytic chamber was diluted by 5.0 mL to be dragged into the scope of the detectable range. 0.1 mL of potassium sodium tartrate tetrahydrate solution (ρ = 500 g·L^{-1}) was added with vigorous mixing, and 0.1 mL of Nessler reagent was injected into the sample in sequence. The absorbance of the yellowish-colorized mixture was recorded at the wavelength of 420 nm after resting for 20 min at room temperature. The calibration curve of absorbance against ammonia-N concentration was derived through the serial diluted standard solutions of ammonium chloride solution, and before that, the ammonium chloride crystal was dried in advance at 105 °C for 2 h.

Measurement of hydroxylamine (NH_3OH^+)-N

The ionic concentrations of hydroxylamine-N presented in electrolytes were determined by the traditional spectrophotometric method by Frear et al [21, 25, 83]. 1.0 mL of the electrolyte was sampled from the electrolytic chamber and mixed with 1.0 mL of phosphate buffer (PBS, 0.05 M, pH = 6.8), 0.8 mL of DIW, 0.2 mL of trichloroacetic acid (TCA) solution (12 wt.% in DIW), and 1.0 mL of 8-quinolinol solution (1.0 g of 8-quinolinol in 100 mL of absolute ethyl alcohol). 1.0 mL of sodium carbonate solution (Na_2CO_3, 1 M) was sequentially added, and the final mixed solution was placed in 80 °C of water bath for 1 min. After cooling down for 15 min at room temperature, the absorbance of the greenish-colorized mixture was recorded at the wavelength of 705 nm. The calibration curve of absorbance against hydroxylamine-N concentration was derived through the serial diluted standard solutions of the commercial hydroxylamine solution.

Calculation of yield and FE of NH_3

After implementing the electrochemical reduction reaction of NO-to-NH_3, the yield of NH_3 was calculated by the equation as follows

$$\text{Yield}_{NH_3} = \frac{c_{NH_3} \times V}{M_{NH_3} \times t \times S}$$

where c_{NH3} is the mass concentration of NH_3 (g·L^{-1}), V is the total volume of cathode chamber (L), M_{NH3} is the molar mass of NH_3 (17 g·mol^{-1}), t is the electrolysis implemented time (s), and S is the geometric area of working electrode (1 cm^2) [23, 70].

FE for product A was respectively calculated according to the equation as follows, herein, product A is of electrochemically synthesized NH_3 and NH_2OH

$$\text{FE}(\%) = \frac{n_A \times F \times c_A \times V}{M_A \times Q} \times 100$$

where n_A is the electron number for A generation (n = 5 for NH_3, and n = 3 for NH_2OH), F is the Faraday constant (96,485 C·mol^{-1}), c_A is the mass concentration of A (g·L^{-1}), V is the total volume of cathode chamber (L), M_A is the molar mass of A (NH_3: 17 g·mol^{-1} and NH_2OH: 33 g·mol^{-1}), and Q is the total charge passing through the electrode [23, 70].

Differential electrochemical mass spectrometry experiments

The *in-situ* online analysis for electrochemical reduction reaction was conducted by differential electrochemical mass spectrometry (DEMS, HPR-40, Hiden analytical, UK). NO gas saturated 0.1 M HCl electrolyte was circulated with a circulating rate of 2 sccm, and LSV with the potential range of +0.5 to −0.8 V vs. RHE and CA test at +0.1 V vs. RHE was respectively carried out. The mass signals of N-containing products (NH_3, NH_2OH, N_2, N_2O, and N_2H_4) and H_2 were simultaneously recorded. Detecting of the mass signals by CA test with the electrolyte of not gaseous NO reactant but 10 mM of NH_2OH was additionally performed to identify the reduction reaction pathways [81].

Isotope labeling experiments

The isotope labeling experiment was carried out using ^{1}H nuclear magnetic resonance (^{1}H NMR, Bruker 600-MHz system) with ^{15}NO as the feeding gas. ^{15}NO was experimentally synthesized with the reaction as follows [23]

$$3Na^{15}NO_2 + H_2SO_4 \rightarrow 2^{15}NO(g)\uparrow + Na^{15}NO_3 + Na_2SO_4 + H_2O$$

100 mL of 1 M H_2SO_4 prepared in the Teflon bottle with a rubber cap was pre-degassed with helium gas for at least 30 min with the 20 sccm of flow rate, and 0.5 mL of 7.4 M $Na^{15}NO_2$ was added with installing gas sampling bag at the outlet line. This as-prepared ^{15}NO gas was confirmed by gas chromatograph (GC-9790 Fuli Analysis Apparatus Co., China).

Simultaneously injecting Ar through the Teflon bottle continuously, all produced gases were directly moved toward the cathodic chamber and participated in the reduction reaction as a ^{15}NO feeding gas to the electrochemical cell. The actual reaction of ^{15}NO-to-NH_3 was conducted with the same H-type electrolytic quartz cell filled with 50 mL of 0.1 M HCl (pH = 1) electrolyte, and the electrolysis test was conducted at +0.1 V vs. RHE for 1 h. The ^{15}N-contained ammonium ions ($^{15}NH_4^+$) in electrolyte samples were detected by NMR as follows: (1) adding 20 mg maleic acid to 50 mL of resultant electrolysis, and (2) adding 50 μL of D_2O to 0.5 mL of the above-prepared mixture. The standard curve of $^{15}NH_4^+$ was derived by the ratio of peak area of $^{15}NH_4^+$ over maleic acid of the standard solution, prepared by 5 steps serial-diluted standard solution with the concentration from 100 to 3.1 mM of $^{15}NH_4Cl$. The linearly correlated standard curve was obtained, thus the electrochemically synthesized $^{15}NH_4^+$ was quantified by following the induced standard equation.

2.6 Theoretical calculation

To get the model of the defective BNC monolayer with Au embedment, a supercell containing carbon atoms, Au atoms, B atoms, and N atoms with a vacuum of at least 15 Å was set up [32], where the ratio of the number of atoms is determined by XPS. Calculations had been conducted by DFT with the projector augmented wave method using the Vienne *ab initio* simulation package (VASP) [23]. The generalized gradient approximation (GGA) was designed by Perdew–Burke–Ernzerhof (PBE) with van der Waals correction to optimize their geometric structure, and the convergence criteria for energy and force were applied as 10^{-5} eV and 0.02 eV·Å^{-1}, respectively [21, 23]. One-half of the chemical potential of hydrogen as the chemical potential of the proton-electron pairs; $\mu(H^+) + \mu(e^-) = \frac{1}{2}\mu(H_2(g))$ [21, 23], was used as the computational hydrogen electrode model [21, 23]. In addition, ΔG value was computed as follows

$$\Delta G = \Delta E + \Delta E_{ZPE} + \Delta G_U - T\Delta S$$

where ΔE is the electronic energy difference induced from DFT calculations, ΔE_{ZPE} is the zero-point energy change, ΔG_U is the free

energy contribution corresponded by the applied electrode potential (U), T is the temperature (298.15 K), and ΔS is the change in entropy [21].

3 Results and discussion

3.1 Characterization of Au-BNC catalyst

Figure 1(a) illustrates the synthesis process and the fabrication structure which is fostered with the BNC with metallic nanoparticles of Au (Au-BNC). The basic backbone structural carbon of N-doped CNT (noted as NC) comprised of carbon polymer of PEG-2000 [41], and urea as a reductant and N-dopant. Boric acid (H_3BO_3), a critical component in the reaction, was added to prevent Au agglomeration and provide a B-heteroatom source for co-doping with NC, and the addition of $HAuCl_4{\cdot}3H_2O$ embeds the metallic Au catalyst, creating the active reaction site. The macro-scaled structure of MF was mixed with the prepared precursors and dried in the oven at 80 °C after sufficient stirring for 24 h under ambient conditions; during this process, Au ions were instantly embedded as it was and neutralized to metallic Au nanoparticles, and H_3BO_3 was dehydrated to B_2O_3 [84]. All mixtures uniformly adhere to the melamine structure, and during the pyrolysis process at 900 °C, B- and N-dopants are implanted to the CNT by substituting carbon atoms within the graphene patterns, while metallic Au stably settles on newly created defects. The final Au-BNC containing Au nanocrystals is eventually prepared after rinsing out B_2O_3 foreign matter with ethanol and DIW repeatedly. The ESM provides a detailed account of the materials, preparation procedures, analysis, characterization, and calculation.

Figure 1(b) and Fig. S3 in the ESM show TEM and FESEM images of BNC and Au-BNC, which reveal a hollow fiber array morphology in CNT. The Au nanoparticles are uniformly dispersed on the amorphous BNC support (Fig. 1(c)) with an average size of 32.5 nm (Fig. 1(c), inset). The high-resolution TEM (HRTEM) image in Fig. 1(d) shows that the particles have good crystallinity with lattice fringes of 0.143 nm, corresponding to the (220) facet of Au, and the selected-area electron diffraction (SAED) pattern in the inset of Fig. 1(d) confirms this result. The powder X-ray diffraction (pXRD) of Au-BNC in Fig. 1(g) shows three significant peaks of 2θ diffraction at 38.2°, 44.5°, and 64.8° corresponding to gold facets of (111), (200), and (220) respectively (JCPDS No. 4-0784) [58, 70] and two broad peaks at 26° and 44° originated from the backbone graphene [21, 58]. The corresponding elemental mapping image intuitively shows a homogeneous distribution of the C, N, B, O, and Au nanoparticles on BNC, herein, the wall of CNT has marked as blue coloring carbon with high dense (Fig. 1(f)). The presence of Au SAs is double confirmed by HAADF-STEM, indicating no verifiable trace of Au single atom is identified within BNC (Fig. 1(f)) [27]. The N_2 adsorption–desorption test was carried out (Fig. 1(h) and Table S1 in the ESM) to exhibit the pore structure of the catalyst, with isotherms for BNC and Au-BNC ascribed to a type-IV hysteresis loop. The specific area BCN and Au-BNC are 612.2 and 483.4 $m^2{\cdot}g^{-1}$, respectively, with pore size distribution divided into mesopores (~ 4.0 nm) and micropores (~ 1.9 nm), as shown in the inset of Fig. 1(h). The CNT morphology serves as a base structure, with the isotherm under high relative pressure indicating multi-layer adsorption, and the pore size distribution corresponding to the complexity of macro-structure by MF and micro-structure by

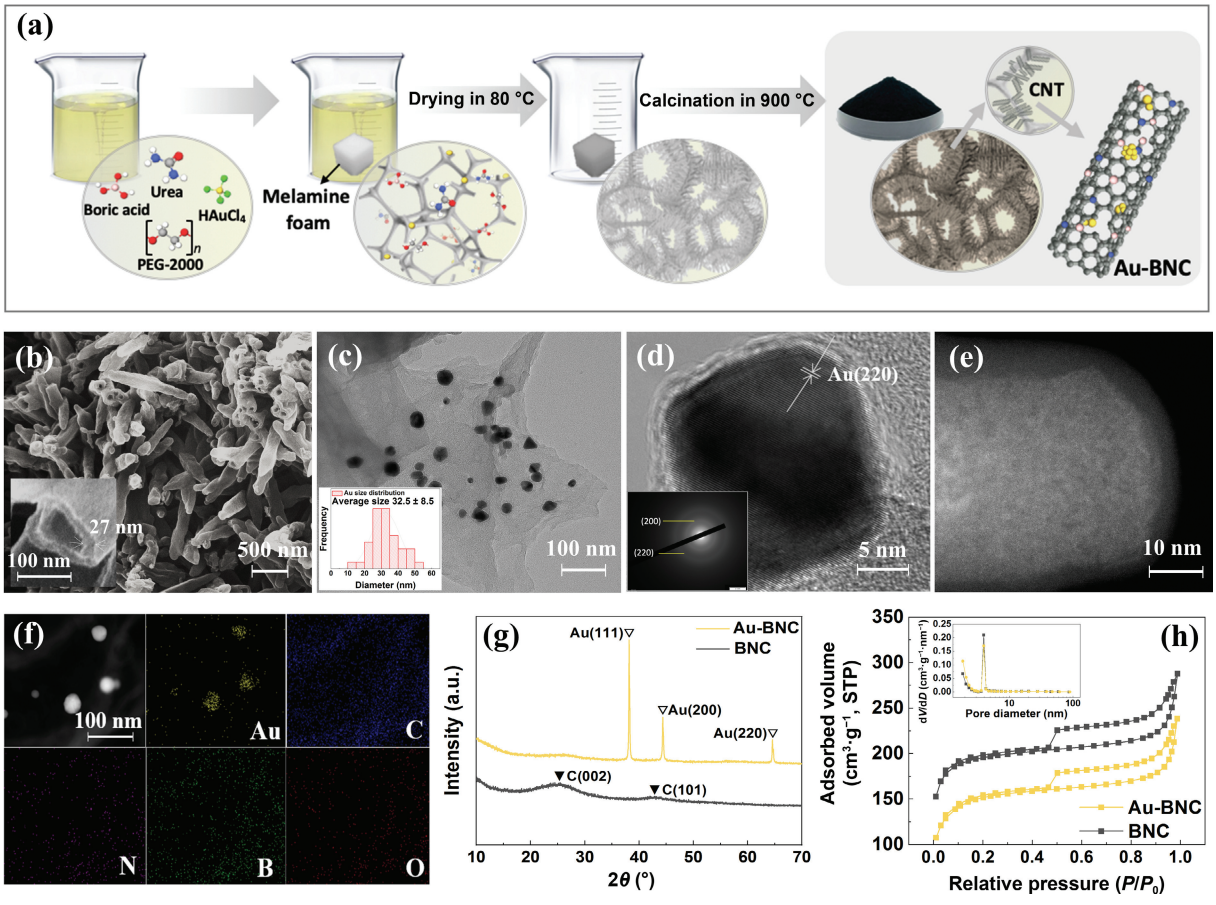

Figure 1 (a) Illustration of the preparation of Au-BNC catalyst. (b) FESEM image of Au-BNC and the width of CNT (inset). (c) TEM image of Au-BNC and Au nanoparticle size distribution (inset). (d) HRTEM image of Au-BNC and SAED pattern of Au nanoparticle (inset). (e) HADDF-STEM image of Au-BNC. (f) EDS mapping images visualizing the actual Au nanoparticles on the BNC. (g) XRD patterns of Au-BNC and BNC. (h) BET curves of Au-BNC and BNC and pore size distributions (inset).

CNT.

To understand the role of B-dopant on the NC, with the reasonable hypothesis enhancing dispersibility of the actual catalytic active site of Au and editing the defect sites on graphene by modifying the bonds and electron distribution, originated by the extra addition of the B-dopants, the structural electronic properties, and surface characterization were conducted. With the same amount of 0.4 mM Au atom, the specific structure differences caused by B-doping are confirmed only by manipulating the presence of B-heteroatom. ATR-IR spectra of Au-BNC and Au-NC (Fig. 2(a)), revealing that the addition of B-dopants definitively alters the bonding structure of NC. ATR-IR, scanning range with 400–4000 cm^{-1}, exhibited the outstanding peaks attributed to graphene at 3430 cm^{-1} (C–OH), and nitrogen concerned bond at 3260 cm^{-1} (N–H), 1543 and 1244 cm^{-1} (C–N) [43, 85, 86]. By contrast, five additional new peaks appear in the spectrum of Au-BNC at 1626, 1400, 1171, 1080, 890, and 796 cm^{-1}, assigned to C–B, N–B, C–B, C–B, B–O, and N–B in sequence, stretching of B-doping on the pristine NC [87, 88]. While the conventional peaks with C and N are somewhat obscured by the new peaks with C–B, B–O, and N–B, they confirm the presence of B-doping in the carbon network and provide visible evidence for the incorporation of B atoms in the NC [89].

The incorporation of B-modification into NC creates more defect sites, which could directly impact the properties of Au embedment. As shown in Fig. 2(b), the Raman spectra of both Au-BNC and Au-NC display peaks at 13181567 and 1567 cm^{-1} corresponding to D-band and G-band, which indicated the defective/disordered carbon and the sp^2-hybridized/crystalized graphitic carbon atoms, respectively [21, 32]. The character of the defect level in the graphitic structure could be assessed by the intensity ratio of (I_D/I_G) [90], herein, the I_D/I_G value increases from 1.27 to 1.65 after B-doping, indicating a lower graphitic structure and confirming the increased defect level of Au-BNC. The EPR analysis (Fig. 2(c)), which possesses an asymmetric signal line centered at g = 2.003, indicated the presence of unpaired electrons on the π-conjugated structure [91–94]. With the addition of B-dopant on NC, the intensity of the EPR peak is strengthened as a result of an increase in the number of N-defect sites, so allowing to provide a plenty embeddable site of a metallic nanocrystal of Au through redistribution of electron density at the adjacent site of the N-defect, BNH_2 [58, 89, 95–99]. At the same time, the B-dopant neighboring with N-defect becomes serving under-coordinated sites, that of electron acceptors, tailoring it to be an active site that is more receptive to electron-donating reactants in nature [100–102].

XPS survey spectra of Au-BNC and Au-NC exhibit significant changes in the atomic portions of O, N, C, B, and Au (Fig. 2(d) and Table S2 in the ESM). While under the co-doping of B and N, heteroatoms are competitively implanted on graphene, but originally, the substitutional doping of B has more preferably occurred over the in-plane N doping [54, 103]. In-plane substitutional B-dopant (BC_3) is notably visualized in Fig. S4(e) in the ESM, exhibiting more stable sp^2 hybridization in graphene accompanied by retaining planar structure [104]. The electron-deficient B atom polarizes with the neighboring graphitic sites by altering the C atoms, forming a B–C bond (~ 1.50 Å) that is longer than a C–C bond (~ 1.40 Å) in the pristine graphene [104–106]. Simultaneously, the significant increase of N peak in XPS spectrum (Fig. 2(d)) reveals a new appearance of the N-related bond with B-dopant, which could be occurred by dragging of B rather than C toward N owing to the weaker electronegativity of B (2.04) than C (2.55), forming B–N hybridized domain of B–N–C on graphene [107]. The resultants of N 1s and B 1s

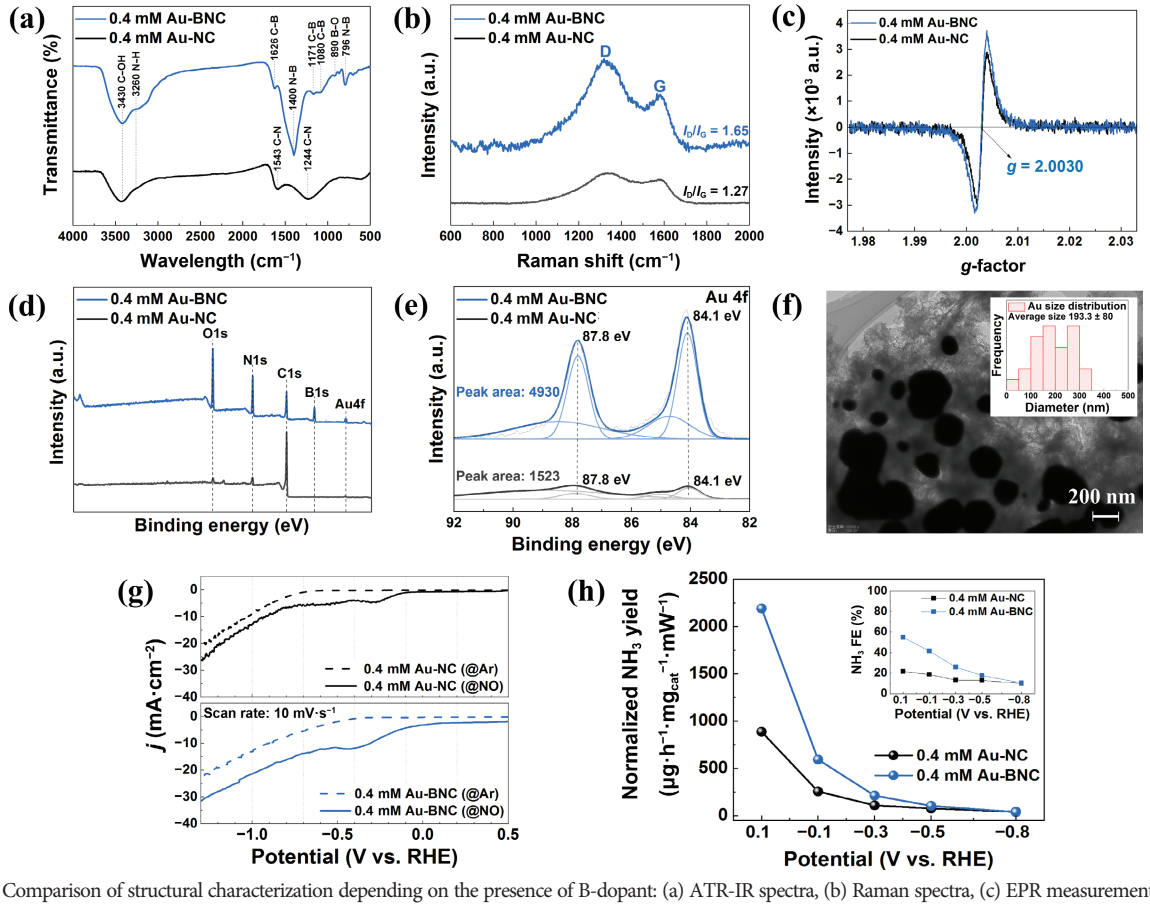

Figure 2 Comparison of structural characterization depending on the presence of B-dopant: (a) ATR-IR spectra, (b) Raman spectra, (c) EPR measurements, (d) XPS survey spectra, and (e) XPS spectra of Au 4f. (f) TEM image of Au-NC and pore size distribution (inset). (g) Linear sweep voltammetry scans of Au-BNC and Au-NC. (h) Normalized NH_3 yield and faradaic efficiency (inset) under various potential with Au-BNC and Au-NC.

spectra exhibit significant B–N hybridized domains located at the peak positions of 397.8 and 192.2 eV [21]. In addition, under proceeding pyrolysis, the strong radical of B_2O_2 can directly participate in creating the bonds of B–O and C–O favorably, rather than C–N bonds [108]. These changes in the bond portion are reflected in XPS consistently with the stretching bond of the newly introduced B–N, B–O, and C–OH, as shown in the ATR-IR spectra. The high-resolution C 1s spectrum of Au-BNC resolves into seven peaks in XPS (Fig. S4 in the ESM) and shows a higher sp^3/sp^2 ratio than Au-NC, indicating a decrease in catalytic conductivity. The new appearance of the π–π* peak (291.8 eV) formed by sp^2-hybridization which indicates the availability of π-conjugate delocalized electrons offset the graphitic insulation, and conversely, improved the conductivity of the catalyst [90, 109, 110]. Au 4f XPS spectrum of Au-BNC (Fig. 2(e)) exhibits a doublet with binding energies shifted to a more positive range: 84.1 eV ($Au^{\delta+}_{7/2}$) and 87.8 eV ($Au^{\delta+}_{5/2}$), in contrast to the metallic Au^0 double peaks of 84.0 eV ($Au^0_{7/2}$) and 87.6 eV ($Au^0_{5/2}$) [111, 112]. According to the increase of N-defect with doping B-heteroatom, elemental quantification of Au was increased from 0.08% to 0.20% (Table S2 in the ESM), and the total peak area of Au is also enlarged from 1523 to 4930, indicating an absolute increase in the Au embedment. On the other hand, the average Au particle size is reversely lower to approximately reaching 32.5 nm with Au-BNC, from 193.3 nm with Au-NC, indicating that B-dopant helped in the dispersion of Au nanoparticles widely and regularly, and served as actual seed sites for Au (Fig. 2(f)). Largely agglomerated Au at the catalyst having no B-heteroatom hinders the stable construction of hollow fiber form of CNT, so it displays the lumped structure and even shows multi-layer graphene covering the bulk-sized Au nanoparticles (Fig. S3 in the ESM).

3.2 NORR performance and mechanism with Au-BNC

The measurement of NORR performance was carried out in an H-type cell at room temperature and atmospheric pressure (Fig. S5 in the ESM). First, LSV was performed while supplying Ar and 99.9% high-purity NO gas directly to a working electrode in 0.1 M HCl electrolytes with a flow rate of 20 sccm. Both catalysts exhibit NORR activity, but notably, the presence of B-dopant results in a higher current density increase at the final potential of −1.3 V vs. RHE, up to 5.2 $mA{\cdot}cm^{-2}$ (Fig. 2(g)). The NORR performances of each catalyst were examined through CA for 2 h under the potential range from +0.1 to −0.8 V vs. RHE (Fig. S6 in the ESM). The amount of NH_3, in the form of NH_4^+, was measured with the Nessler reagent method (Fig. S7 in the ESM), and all yields of NH_3 were normalized to the value corresponding to the amount of power density at each potential. The normalized yield and FE of NH_3 decreased as the potential increased, attaining a maximum value reaching 2220 $\mu g{\cdot}h^{-1}{\cdot}mg_{cat}^{-1}{\cdot}mW^{-1}$ and 59% at +0.1 V vs. RHE with Au-BNC, which contains 0.4 mM of Au (Fig. 2(h) and Fig. S8 in the ESM). The advancement in spontaneous affinity between the reactant (or reaction intermediate) and the B-doped catalytic electrode is responsible for approximately 3.7 times higher yield of NH_3, as evidenced by the adlayer peak current density in Fig. 2(g) [113]. The Adlayer peak currents are prominently exhibited in the acidic electrolyte, as depicted in Fig. S9 in the ESM. Furthermore, the catalytic performance of the B-doped catalyst is demonstrated to enhance the FE of NH_3 synthesis, detected below the onset potential. This observation suggests that a greater number of H^+ species are involved in the selective synthesis of NH_3, with a comparatively reduced tendency towards H^+ reduction to H_2. The difference in adlayer peak currents observed in the LSV graphs measured under different pH conditions, in the absence of the reactant NO, clearly substantiates the H^+ suppression effect induced by the B-dopant (Fig. S10 in the ESM). In acidic electrolytes, the presence of B, with its positive nature, leads to a thinner double layer due to the repulsion of H^+ ions. Conversely, in alkaline electrolytes with 0.5 M of KOH, B-dopants attract OH^- ions, resulting in a stark thicker double layer compared to the condition without B-dopant. This provides a more pronounced evidence for the H^+ suppression phenomenon caused by the B-dopant.

To obtain deep insights into the NO-to-NH_3 mechanism, the surface reduction pathway over the Au-BNC was calculated by employing DFT computations [114]. First, the adsorption of gaseous NO on Au-BNC was investigated as a prerequisite description for the NO-to-NH_3 [21, 24, 115]. As displayed in the inset of Fig. 3(a), a larger electron cloud exists between NO and Au-BNC, indicating their enhanced interactions and NO gas can be strongly absorbed on the Au-BNC surface. The interaction effect between Au nanoparticles and a NO molecule was further studied by computing the partial density of states (PDOS). As proved by the PDOS in Fig. 3(b), well-matched energy between 4d orbital of Au and π*-orbital of NO indicates the electron transfer to π*-orbital of NO from Au nanoparticles, also corresponding to the result of Bader charge analysis that the modified Au-BNC donated 0.46 and 0.50 e^- to N and O atoms of NO. The structure of Au-BNC and the adsorption model for NO have only been configurated as a side-on configuration with high stability (Table S3 in the ESM). The NO-to-NH_3 was examined in terms of the free energy profiles, particularly in the previous report [24, 66, 115]. For the solvated and coordinated NO, it is easy to be protonated and reduced to single N* based on the standard electrode potential and the DFT results with the Au metallic surface; O-distal pathway is depicted as NO → $NO^*_{(ads)}$ → NOH* → N* + H_2O → NH* → NH_2* → NH_3 (Fig. 3(c)) [24, 66]. Every step for the O-distal pathway is exothermal, implying that the NO-to-NH_3 would be a spontaneous reaction (Fig. 3(a)). This shows high performance in practical application, which is also in agreement with the existence of the adlayer peak current in Fig. 2(g). In addition, as mentioned in previous studies, the intrinsic characteristics of the electron-deficient B-dopant on electrode suppress H* adsorption (under acidic conditions) [52, 116], occurring inferior to the competing reaction of hydrogen evolution reaction (HER), thereby enabling the sufficient proton source to preferentially contribute to NORR [47, 52, 117] and achieving relatively high FEs. In the same vein, the introduction of B-heteroatom results in a noticeable decrease in the onset potential for water reduction, shifting it from −0.72 to −0.52 V vs. RHE (Fig. 2(g)), indicating that the electron depleted site within Au-BNC facilitates the chemisorption of the electron-rich Lewis base molecule of H_2O as well as serves as a catalytic center for occurring the water reduction [41, 52].

3.3 Manipulation Au amounts on BNC

Under the same Au amount of 0.4 mM, depending on the presence of B-dopant, the main peak of XPS Au 4f is maintained at the neutral valence state of Au^0 in spite of increasing the atomic ratio of doping amount. Thus, surface analysis and NORR activity were implemented to investigate the structural mechanism for NH_3 synthesis by manipulating the Au loading amounts on the BNC support (Fig. 4(a)). A series of Au-BNC catalysts with varying Au loading amounts from none to 0.6 mM were prepared. The resulting pXRD patterns reveal conspicuously humped 3-peak corresponding to the Au facets (JCPDS No. 4-0784) (Fig. S11 in the ESM). The actual Au loading on the BNC surface is quantified to be < 0.01 wt.%, 0.155 wt.%, 0.398 wt.%, 3.09 wt.%, 6.46 wt.%, 9.64 wt.%, and 14.40 wt.% in sequence by ICP-OES, showing a well-matched correlation with the atomic portion of Au measured by XPS (Fig. S12 in the ESM).

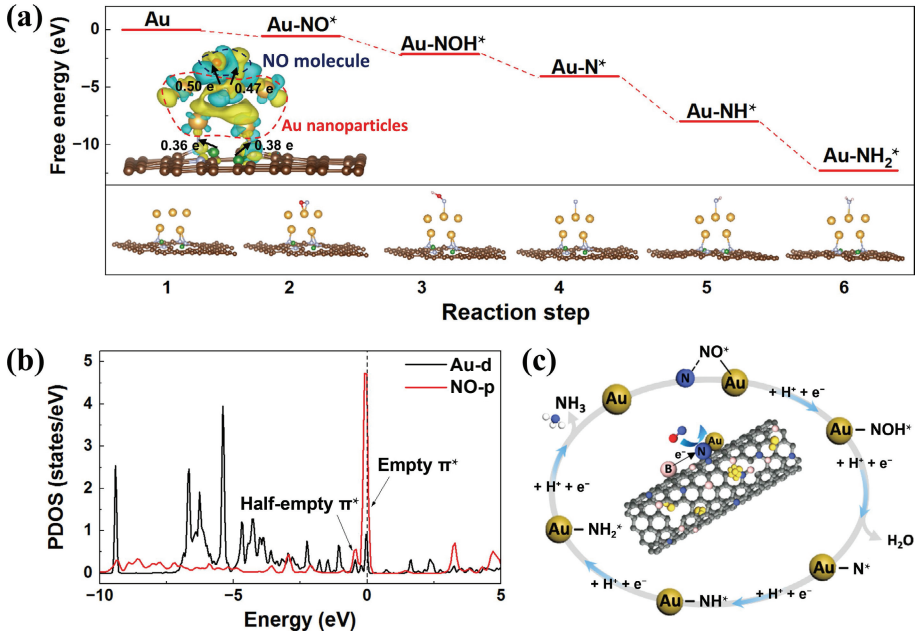

Figure 3 (a) Intermediates and calculated Gibbs free energy diagrams of the NO-to-NH_3, charge density distribution within Au-BNC, showing yellow (electron-rich region) and cyan (electron-deficient region) (inset). (b) PDOS of NO gas molecule on Au-BNC. (c) Schematic illustration of the possible reaction pathways of the NO-to-NH_3.

In the XPS N 1s (Fig. S13 in the ESM), the N–Au peak significantly appears at 399.8 eV by adding Au embedment [21]. On the other hand, the valence states of Au precursor are tuned according to the embedding amount (Fig. 4(b)). At the low embedding level of Au, Au could be tailored within the graphene by bonding with the boric acid originated oxygen species (O_2^{2-} and O^-), leading to the positive valence state of $Au^{\delta+}$ in B–O–$Au^{\delta+}$ bond, and acting as a Lewis acid and triggers for reducing reaction [118], which is deconvoluted as $Au_{5/2}^{\delta+}$ and $Au_{7/2}^{\delta+}$ centered at 88.8 and 84.2–84.6 eV (Fig. 4(c)) [119, 120]. Herein, the elemental peak portions have been preserved similarly with the pristine BNC, and the heteroatom doped structures of graphitic-N (401.0 eV) and N–B (398.0 eV) still are maintained (Figs. S14(a) and S13(b) in the ESM) [41]. In addition, the complementary decrease of pyrrolic-N (399.3 eV) [21] compared with N–Au showed a new bond of Au atoms on N- defect sites where adjacent to the B-doped sp^2 carbon lattice [111, 121–123]. As the result of the DFT calculation, Au directly bonding with B-dopant is rather to be unstable, and bonding only with nitrogen was stable (Table S3 in the ESM). In accordance with the increase in the amount of Au precursor, while the peak spectra for B, N, and O are prominent, the valence states of Au are dragged to the more neutralized state, contributing to the peak centered at 88.0 and 84.2 eV [84]. Au ions spontaneously react with a strong reductant of urea, forming N–$Au^{\delta+}$, and spontaneously react with boric acid to produce B–N–$Au^{\delta+}$ structural bonds, or immediately embed into the B- dopant substituted graphene. Due to this, in the catalysts in which the Au precursor is added at a concentration of Au over 0.1 mM, the graphite-N bond is lost and the N–B bond complementarily increases (Fig. S13(b) in the ESM). Au embedding paths have simultaneously occurred, but the agglomeration of the embedded Au with the neighboring Au and excessive Au precursors diffuses toward the surface of BNC, forming neutral-charged Au nanoparticles as exhibiting peaks positioned close to Au^0 (centered at 87.6 and 84.0 eV for $Au_{5/2}^0$ and $Au_{7/2}^0$ respectively) [111]. As expends the counts of Au nanoparticles on the surface, by the physical interference, the structurally unstable B–C bond would be priory broken than C–C, shown in the decrease of the B–C bond in Fig. S14(b) in the ESM. Even though the different valent states of Au, as noted in the significant crystalline Au peaks in XRD (Fig. S11 in the ESM) and no detection of Au single atom by HADDF-STEM (Fig. 1(e)), every Au-BNC catalyst contains nanoparticles having Au^0–$Au^{\delta+}$ on BNC [118].

3.4 NORR performance by manipulating Au amount

The electro-catalytic activity of Au-BNCs for NORR was investigated in 0.1 M HCl electrolyte, with a scanning potential range from +0.5 to −1.3 V vs. RHE with a scan rate of 10 mV·s^{-1}. In the LSV curve shown in Fig. 5(a), all the Au-loaded BNC catalysts exhibit conspicuous adlayer peak currents below the NORR onset potential of −0.08 V vs. RHE, elucidating the presence of reactants or reaction intermediates chemisorbed on the electrode surface with high affinity [113]. The adlayer peak current is observed only under the NO atmospheric condition with other conditions being identical, suggesting that NO is the only adsorbate bound to the catalytic working electrode surface, denoted as $*NO_{(ads)}$. The amount of adsorbed NO showed an identical trend with the ratio of pyrrolic-N, implying NO is representatively adsorbed on N-defects, thus the NO adsorbing amount is determined not by the amount of Au precursor but by the portion of N-defects. As shown in Fig. 5(b), the trend of the current density at the final potential of −1.3 V vs. RHE is also identical to that of the adlayer peak current density, so it could be elucidated that expediting the affinity of the reactant and reaction surface affected the overall electrical conductance for the catalytic electrode.

The EDLC were calculated by measuring polarization curves at various scan rates from 100 to 10 mV·s^{-1} (Fig. S15 in the ESM). The relation between the average peak current of anodic and cathodic as a function of the scan rate indicates the depletion rate of the reactant on the catalytic electrode, depending on potential changes, and also supports to identify of the major reason for surface reaction limitation [23]. Every catalyst shows a good linear dependence of $(J_a - J_c)/2$ on ν, implying that the NORR in the electrolyte is diffusion-controlled within the potential window [21, 23]. The values of the C_{dl} are grouped by the order of magnitude; herein, every catalyst embedded with Au showed higher electrochemical active surface area than none of Au on BNC (denoted as no Au-BNC), and the EDLCs are increased correspondingly as increasing the valence state of Au [93].

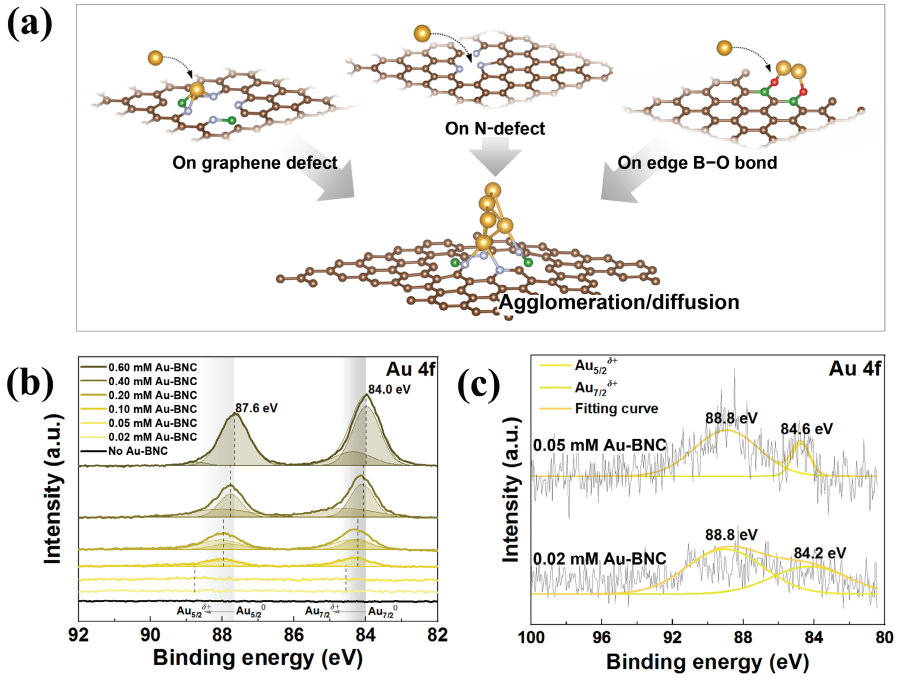

Figure 4 (a) Schematic of the Au nanoparticle embedment mechanism on BNC. (b) Au 4f XPS spectra for Au-BNC with different concentration of Au on BNC. (c) Au 4f XPS spectra for low concentration of 0.02 mM Au-BNC and 0.05 mM Au-BNC.

Specifically, the Au-BNC with the positive valence of $Au^{\delta+}$ had C_{dl} values of 1740 and 3120 μF·cm^{-2} for 0.02 and 0.05 mM Au-BNC, of the three-order of magnitude higher capacities than no Au-BNC (2.21 μF·cm^{-2}), revealing the superior intrinsic activity of Au valence, not stemming from the Au embedded amount [93, 124]. Although the quantities of the embedded Au are proportionally increased (Fig. S12 in the ESM) and the average particle size of Au is non-comparably similar (Fig. S16 in the ESM), only the valence state of Au nanoparticles has an effect on the EDLC. The electrochemical reaction process and electron transfer rate are identified by observing CV and comparing the catalytic resistances by EIS curves (Fig. S18 and Table S4 in the ESM). As demonstrated in Fig. S18(c) in the ESM, the current peak points at the redox potential for all Au-BNCs are lower compared to those of no Au-BNC due to the adhesion of a certain substrate onto the electrode, which disturbs the electron transfer rate [58]. Nonetheless, the Au-BNC with 0.02 and 0.05 mM of Au, containing the positively charged $Au^{\delta+}$ nanoparticles, promotes the acceleration of electron transfer for NORR.

The Nyquist plots shown in Fig. S18 in the ESM illustrate the interfacial processes between the electrode and electrolyte, which consist of a semicircle portion corresponding to electron-transfer resistance (R_{et}) at high frequencies, and a linear portion reflecting diffusion at low frequencies [125]. The increase in R_{et} as the Au embedment proceeded clarifies the stable settlement of the Au nanocomposites on BNC since the promotion of non-polarized neutral Au nanocrystals on the electrode fundamentally limits electron transfer with low electrical conductivity [126]. The value of R_{et} for 0.02 mM Au-BNC has much lower resistance (~ 10.5 Ω) than the more Au-embedded catalysts, which reaches up to 193 Ω, indicating superior electron transfer and better electrical conductivity [58]. The observed trend is consistent with the CV data presented.

Prior to conducting the 2 h electrolytic cell test, retention stages were performed at open circuit potential (OCP) corresponding to each catalyst (Fig. S19(a) in the ESM) for a specified period, allowing for the elimination of any background interferences caused by electrolyte and electrode surfaces [21, 115]. The current density response for the CA test with a specific catalytic electrode of 0.02 mM Au-BNC is negligible, and the accumulated NH_3 is out of the detectable range by UV–vis spectrophotometer (Fig. S19(b) in the ESM) [113, 127]. The actual performances of NORR were measured with each catalyst electrode ranging from none to 0.6 mM Au-BNC via CA at a constant potential for 2 h; the accumulated amount of NH_3 and hydroxylamine (NH_2OH) in the electrolyte (present in the form of electrolyte-soluble ions of NH_4^+ and NH_3OH^+) were detected and FEs were calculated in accordance with the detailed method outlined in the ESM. The NH_3 yield reaches 1877.4 μg·h^{-1}·mg$_{cat}^{-1}$ at −0.8 V vs. RHE at its highest, and the FE for NH_3 at +0.1 V vs. RHE is demonstrated to be up to 94.7% with the catalytic electrode of 0.02 mM Au-BNC (Fig. 5(c)), while the FE for NH_3 is coherently decreased with every catalyst as following the potential increment (Fig. S20 in the ESM).

The observation that each catalyst exhibits enhanced NH_3 selectivity at a potential +0.1 V vs. RHE (Fig. 5(d)) reveals that Au is the actual reaction site and proves the influence of electrochemical characteristics of the adlayer peak current on NORR yield. In order to identify whether NH_2OH could be a candidate as an intermediate reactant throughout the reaction pathway of NO-to-NH_3, subsidiary experiments involving NH_2OH reduction reaction were conducted and the mass signals responding to all N-containing products were analyzed by the online DEMS (Fig. S21 in the ESM). The results represent that no NH_3 product is detected from NH_2OH reduction, suggesting that the two reduction reactions follow independent mechanisms [128] and that the formation of NH_2OH during NORR is not the dominant response.

In order to investigate the factors contributing to the selectivity of NORR toward NH_3 synthesis, we measured the Tafel plots for each catalyst and present the results in Fig. S22 in the ESM. All other slopes with the Au nanocrystals embedded in BNCs are lower, manifesting faster intrinsic kinetics of the catalytic electrode for the first-electron transport to the adsorbed NO* species [129], while the slope for the no Au-BNC catalyst reaches 71 mV·dec^{-1} in NORR. The induced slopes that are close to the theoretical NORR value (60 mV·dec^{-1}) [25, 33] demonstrate profoundly fast NORR kinetics of NO* to NOH* [69]. There was previous research

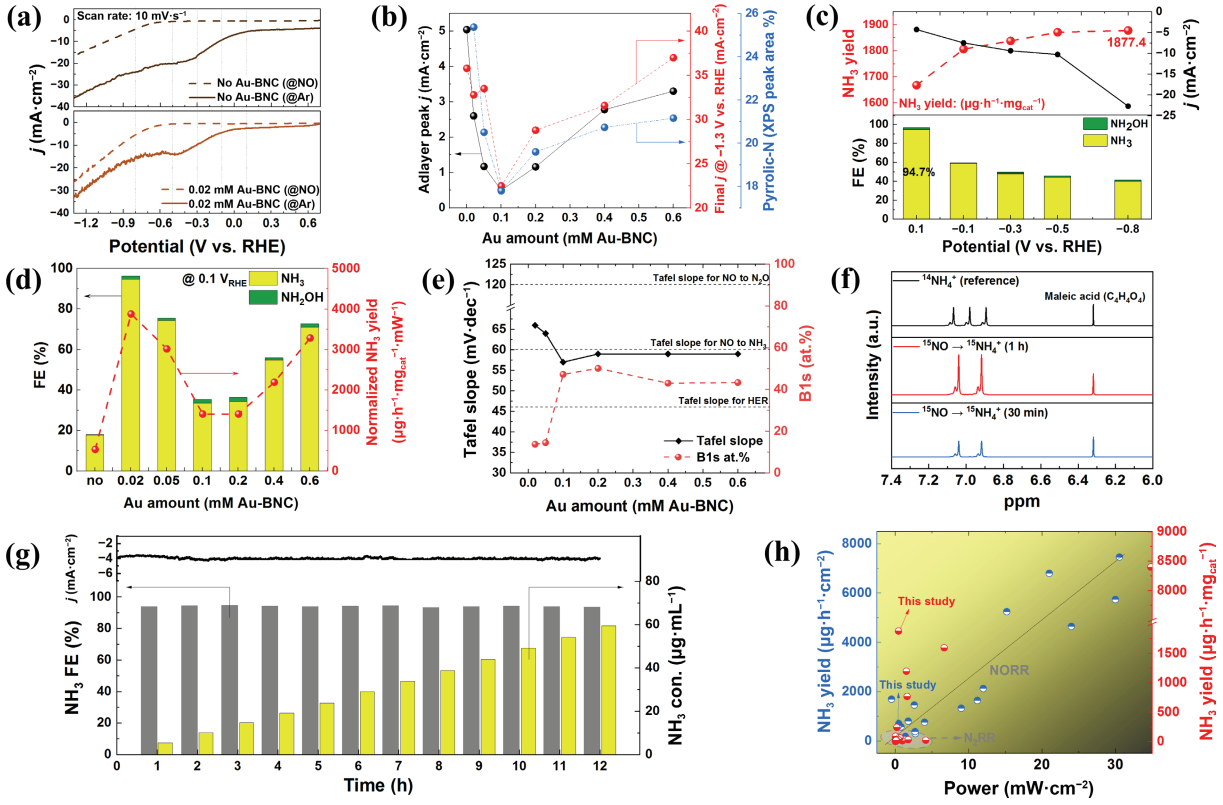

Figure 5 (a) Linear sweep voltammetry scan of no Au-BNC and 0.02 mM Au-BNC under Ar or NO atmosphere, (b) adlayer peak current densities and final current densities reaching at −1.3 V_{RHE} with Au-BNCs, (c) average current density (black line) and the yield of NH_3 (red dots) by chronoamperometry 2 h test at the specific potential range, and electrochemical NORR performance of FEs (bar graphs at the below), (d) FE and the NH_3 yields normalized by power density with Au-BNCs, (e) symmetric reverse relation between the Tafel slopes of Au-BNCs and the atomic content of B-dopant, (f) ^1H NMR spectra of $^{15}NH_4^+$ in electrolytes after NORR from ^{15}NO and reference peak of $^{14}NH_4^+$, (g) NO-to-NH_3 long-term durability test for 12 h with 0.02 mM Au-BNC, and (h) comparison of NH_3 yields with the recent studies from 2017; N_2RR and NORR.

reporting its inferiority in NO* adsorption compared to the competitive H* adsorption that occurs in HER [128]. However, by observing the significant decrement of the Tafel slope by adding B-dopant, from 110 mV·dec^{-1} (0.4 mM Au-NC) to 59 mV·dec^{-1} (0.4 mM Au-BNC), the positively induced B-dopant on BNC is shown to play a role in attracting electron pairs on the NO molecule [91, 130], repulsing H* at the same time, and assisting in conveying the adsorbate of NO* to the active site of Au catalyst. In fact, the trend for the Tafel slope is displayed asymmetrically in reverse with the atomic content of B atoms, revealing that transferring electrons to the adsorbed NO* from Au catalyst has to get affected by B-dopant (Fig. 5(e)). This observation is also in agreement with the result of Bader charge analysis as shown in Fig. 2(g).

Previous studies have referred that the electrochemical reduction of nitrogen reductant based on Au has the propensity to produce N–N coupling dimers (e.g. N_2, N_2O, and N_2H_4) as by-products [69]. Upon detecting molecular intermediate and products over NO-to-NH_3 through the online DEMS at the potential range from +0.5 to −0.8 V vs. RHE, the products of H_2, NH_3, N_2, NH_2OH, and N_2O (*m*/*z* signals of 2, 17, 28, 33, and 44) are observed with every Au-BNC, regardless of the valence states of Au (Fig. S23 in the ESM). A prominent peak of N_2O is exclusively detected with B- doped Au-BNC, attributable to the attraction of NO gas and consecutive adsorption of it on the N-defect, neighboring with B-heteroatom. In addition, N_2 signal detection supports the assumption that N* is generated as an intermediate material during NORR, and for Au, which is an actual reaction site for adsorbing N* (Fig. S24 in the ESM). When Au is excessively doped, the adsorbed intermediates cause the conjugations occurring N–N dimers according to the reaction of adjacent NO* and N*. The absence of response in the overall signal of the N–N dimers derivative upon a constant potential of +0.1 V vs. RHE (Fig. S25 in the ESM), on the contrary, is an ancillary reaction indicating that electrons other than those involved in the FE of ammonia synthesis are consumed in the formation of HER or a minute quantity of NH_2OH.

To ensure that all synthesized NH_3 originated solely from the NORR experimental conditions, a ^{15}NO isotope labeling experiment was conducted. After confirming whether the artificially synthesized ^{15}NO gas consisted of real NO gas balancing with helium (Fig. S26(a) in the ESM), corresponding solutions were then analyzed by isotopic ^1H NMR measurement (Fig. 5(f)) [23]. Notably, two typical peaks corresponding to $^{15}NH_4^+$ are apparently visualized, in contrast to the sharp triple peaks observed with $^{14}NH_4^+$ (Fig. S26(b) in the ESM) [115, 118]. The actual concentrations of $^{15}NH^+$ produced for 30 min and 1 h were determined by the standard curve (Fig. S26(c) in the ESM). These results strongly prove that all detected NH_4^+ ions in this research originated solely from the electrocatalytic NORR over Au-BNC.

Continuous bulk electrolysis was conducted for 12 h in 0.1 M HCl using a catalytic electrode, 0.02 mM Au-BNC, which exhibited the highest FE, to assess the durability of the Au-BNC catalyst for long-term NO-to-NH_3 conversion (Fig. 5(g)). For long-term durability testing, a circulating system with 500 mL of electrolyte was employed, with a flow rate of 10 sccm, and 20 mL samples were collected every hour for analysis. The FEs and the accumulated NH_3 concentrations in the electrolyte were monitored hourly using CA. It was observed that the FE remained stable at ca. 92% throughout the operating time, and the accumulated NH_3 concentration shows a linear increase at a synthesis rate of ca. 4.9 μg·mL^{-1}·h^{-1} without any structural degradation (Fig. S27 in the ESM). The slightly lower FE is presumed to be attributed to the diffusion of NH_4^+ concentration caused by electrolyte circulation and changes in the aqueous NO

concentration on the catalytic electrode surface due to flow. These results confirm that the Au-BNC catalyst demonstrates stable electrolytic performance for long-term conversion, with no hindrance observed in NO-to-NH_3 at accumulated NH_3 concentrations below 60 μg·mL^{-1} in the final electrolyte.

Figure 5(h) depicts the NH_3 synthesizing yield, which reaches a maximum of 1877.4 μg·h^{-1} mg_{cat}^{-1} at −0.8 V vs. RHE, representing the highest performance achieved in terms of catalytic weight and yield per power consumption. However, when the yield is normalized by the electrode area, which mostly involves a specialized electrolysis system with a gas diffusion layer or metallic surface electrode, the performance is observed to plateau at an intermediate level. This suggests that there are still opportunities for improving electrolytic performance through the development of novel structural systems and cell configurations.

4 Conclusions

This work has proposed a potential for catalytic application of Au nanoparticles with very high FE reaching 94.7% at +0.1 V vs. RHE, implying the occurrence of spontaneous NO-to-NH_3 mechanism rather than the major competitive reaction of HER under the low potential below onset potential of NORR. Transmitting electrode clouds from B-heteroatom to the adjacent N and Au affects the presence of the adlayer current density, which elucidates the amount of the adsorbable sites for aqueous NO on the catalytic working electrode. And the electron-deficient B-dopant could repulse the approach of H*, exhibiting a high FE for NH_3. The best performance of 1877.4 μg·h^{-1}·mg_{cat}^{-1} at −0.8 V vs. RHE, achieved with the minimum amount of Au embedment and low power consumption, has the potential to exceed the DOE target by over two orders of magnitude. This electro-synthesis of NH_3 by Au with spontaneous catalytic reaction has a promising potential for achieving higher efficiency with low energy, furthermore, showing the possibility of producing valuable products from NO exhausts through continuous aquatic diffusion. Beyond the electro-efficiency based on the valence state of Au nanoparticles addressed in this study, further research is required to explore the properties of Au and their correlation with electro-reduction reaction. Particularly, the size and more detailed distribution of Au have a significant impact on actual electrochemical reactions, therefore, further studies aiming at achieving higher production yields necessitate investigation into the relationship between the properties of Au nanoparticles and electrochemical NO-to-NH_3 conversion.

Acknowledgements

This work was financially supported by the National Natural Science Foundation of China (Nos. 22206096 and 21936005) and China Postdoctoral Science Foundation (Nos. 2020TQ0166 and 2021M691771).

Electronic Supplementary Material: Supplementary material (associated with the details of characterization) is available in the online version of this article at https://doi.org/10.1007/s12274-023-5943-0.

References

[1] Ye, B.; Jeong, B.; Lee, M. J.; Kim, T. H.; Park, S. S.; Jung, J.; Lee, S.; Kim, H. D. Recent trends in vanadium-based SCR catalysts for NO_x reduction in industrial applications: Stationary sources. *Nano Converg.* **2022**, *9*, 51.

[2] Lee, T.; Bai, H. Low temperature selective catalytic reduction of NO_X with NH_3 over Mn-based catalyst: A review. *AIMS Environmen. Sci.* **2016**, *3*, 261–289.

[3] Liang, J.; Chen, H. Y.; Mou, T.; Zhang, L. C.; Lin, Y. T.; Yue, L. C.; Luo, Y. S.; Liu, Q.; Li, N.; Alshehri, A. A. et al. Coupling denitrification and ammonia synthesis via selective electrochemical reduction of nitric oxide over Fe_2O_3 nanorods. *J. Mater. Chem. A* **2022**, *10*, 6454–6462.

[4] Alves, L.; Holz, L. I. V.; Fernandes, C.; Ribeirinha, P.; Mendes, D.; Fagg, D. P.; Mendes, A. A comprehensive review of NO_x and N_2O mitigation from industrial streams. *Renew. Sust. Energy Rev.* **2022**, *155*, 111916.

[5] Koebel, M.; Madia, G.; Elsener, M. Selective catalytic reduction of NO and NO_2 at low temperatures. *Catal. Today* **2002**, *73*, 239–247.

[6] Sharif, H. M. A.; Mahmood, N.; Wang, S. Y.; Hussain, I.; Hou, Y. N.; Yang, L. H.; Zhao, X.; Yang, B. Recent advances in hybrid wet scrubbing techniques for NO_x and SO_2 removal: State of the art and future research. *Chemosphere* **2021**, *273*, 129695.

[7] Zhang, Y. Y.; Cao, G. J.; Yang, X. Advances in De-NO_x methods and catalysts for direct catalytic decomposition of NO: A review. *Energy Fuels* **2021**, *35*, 6443–6464.

[8] Chen, H. H.; Zhang, C. Q.; Sheng, L.; Wang, M. M.; Fu, W.; Gao, S.; Zhang, Z. R.; Chen, S. Q.; Si, R.; Wang, L. Z. et al. Copper single-atom catalyst as a high-performance electrocatalyst for nitrate-ammonium conversion. *J. Hazard. Mater.* **2022**, *434*, 128892.

[9] Tang, C.; Qiao, S. Z. How to explore ambient electrocatalytic nitrogen reduction reliably and insightfully. *Chem. Soc. Rev.* **2019**, *48*, 3166–3180.

[10] Chen, J. G.; Crooks, R. M.; Seefeldt, L. C.; Bren, K. L.; Bullock, R. M.; Darensbourg, M. Y.; Holland, P. L.; Hoffman, B.; Janik, M. J.; Jones, A. K. et al. Beyond fossil fuel-driven nitrogen transformations. *Science* **2018**, *360*, eaar6611.

[11] Galloway, J. N.; Townsend, A. R.; Erisman, J. W.; Bekunda, M.; Cai, Z. C.; Freney, J. R.; Martinelli, L. A.; Seitzinger, S. P.; Sutton, M. A. Transformation of the nitrogen cycle: Recent trends, questions, and potential solutions. *Science* **2008**, *320*, 889–892.

[12] Lv, C. D.; Liu, J. W.; Lee, C.; Zhu, Q.; Xu, J. W.; Pan, H. G.; Xue, C.; Yan, Q. Y. Emerging p-block-element-based electrocatalysts for sustainable nitrogen conversion. *ACS Nano* **2022**, *16*, 15512–15527.

[13] van der Ham, C. J. M.; Koper, M. T. M.; Hetterscheid, D. G. H. Challenges in reduction of dinitrogen by proton and electron transfer. *Chem. Soc. Rev.* **2014**, *43*, 5183–5191.

[14] Wu, T. T.; Fan, W. J.; Zhang, Y.; Zhang, F. X. Electrochemical synthesis of ammonia: Progress and challenges. *Mater. Today Phys.* **2021**, *16*, 100310.

[15] Qing, G.; Ghazfar, R.; Jackowski, S. T.; Habibzadeh, F.; Ashtiani, M. M.; Chen, C. P.; Smith III, M. R.; Hamann, T. W. Recent advances and challenges of electrocatalytic N_2 reduction to ammonia. *Chem. Rev.* **2020**, *120*, 5437–5516.

[16] Chen, H. J.; Liang, J.; Li, L.; Zheng, B. Z.; Feng, Z. S.; Xu, Z. Q.; Luo, Y. L.; Liu, Q.; Shi, X. F.; Liu, Y. et al. Ti_2O_3 nanoparticles with Ti^{3+} sites toward efficient NH_3 electrosynthesis under ambient conditions. *ACS Appl. Mater. Interfaces* **2021**, *13*, 41715–41722.

[17] Li, S. X.; Wu, Y. M.; Liu, Q.; Li, B. H.; Li, T. S.; Zhao, H. T.; Alshehri, A. A.; Alzahrani, K. A.; Luo, Y. L.; Li, L. et al. CuS concave polyhedral superstructures enabled efficient N_2 electroreduction to NH_3 at ambient conditions. *Inorg. Chem. Front.* **2021**, *8*, 3105–3110.

[18] Liu, S. S.; Qian, T.; Wang, M. F.; Ji, H. Q.; Shen, X. W.; Wang, C.; Yan, C. L. Proton-filtering covalent organic frameworks with superior nitrogen penetration flux promote ambient ammonia synthesis. *Nat. Catal.* **2021**, *4*, 322–331.

[19] Yang, B.; Ding, W. L.; Zhang, H. H.; Zhang, S. J. Recent progress in electrochemical synthesis of ammonia from nitrogen: Strategies to improve the catalytic activity and selectivity. *Energy Environ. Sci.* **2021**, *14*, 672–687.

[20] Guo, C. X.; Ran, J. R.; Vasileff, A.; Qiao, S. Z. Rational design of electrocatalysts and photo (electro) catalysts for nitrogen reduction to ammonia (NH_3) under ambient conditions. *Energy Environ. Sci.* **2018**, *11*, 45–56.

[21] Peng, X. Y.; Mi, Y. Y.; Bao, H. H.; Liu, Y. F.; Qi, D. F.; Qiu, Y.;

Zhuo, L. C.; Zhao, S. Z.; Sun, J. Q.; Tang, X. L. et al. Ambient electrosynthesis of ammonia with efficient denitration. *Nano Energy* **2020**, *78*, 105321.

[22] Yang, J.; Qi, H. F.; Li, A. Q.; Liu, X. Y.; Yang, X. F.; Zhang, S. X.; Zhao, Q.; Jiang, Q. K.; Su, Y.; Zhang, L. L. et al. Potential-driven restructuring of Cu single atoms to nanoparticles for boosting the electrochemical reduction of nitrate to ammonia. *J. Am. Chem. Soc.* **2022**, *144*, 12062–12071.

[23] Cheon, S.; Kim, W. J.; Kim, D. Y.; Kwon, Y.; Han, J. I. Electro-synthesis of ammonia from dilute nitric oxide on a gas diffusion electrode. *ACS Energy Lett.* **2022**, *7*, 958–965.

[24] Long, J.; Chen, S. M.; Zhang, Y. L.; Guo, C. X.; Fu, X. Y.; Deng, D. H.; Xiao, J. P. Direct electrochemical ammonia synthesis from nitric oxide. *Angew. Chem., Int. Ed.* **2020**, *59*, 9711–9718.

[25] Ko, B. H.; Hasa, B.; Shin, H.; Zhao, Y. R.; Jiao, F. Electrochemical reduction of gaseous nitrogen oxides on transition metals at ambient conditions. *J. Am. Chem. Soc.* **2022**, *144*, 1258–1266.

[26] Rhimi, B.; Padervand, M.; Jouini, H.; Ghasemi, S.; Bahnemann, D. W.; Wang, C. Recent progress in NO_x photocatalytic removal: Surface/interface engineering and mechanistic understanding. *J. Environ. Chem. Eng.* **2022**, *1*, 108566.

[27] Herzing, A. A.; Kiely, C. J.; Carley, A. F.; Landon, P.; Hutchings, G. J. Identification of active gold nanoclusters on iron oxide supports for CO oxidation. *Science* **2008**, *321*, 1331–1335.

[28] Rosca, V.; Beltramo, G. L.; Koper, M. T. Reduction of NO adlayers on Pt (110) and Pt (111) in acidic media: Evidence for adsorption site-specific reduction. *Langmuir* **2005**, *21*, 1448–1456.

[29] Rosca, V.; Koper, M. T. M. Mechanism of electrocatalytic reduction of nitric oxide on Pt (100). *J. Phys. Chem. B* **2005**, *109*, 16750–16759.

[30] Liu, H.; Xiang, K. S.; Yang, B. T.; Xie, X. F.; Wang, D. L.; Zhang, C.; Liu, Z. L.; Yang, S.; Liu, C.; Zou, J. P. et al. The electrochemical selective reduction of NO using $CoSe_2$@CNTs hybrid. *Environ. Sci. Pollut. Res.* **2017**, *24*, 14249–14258.

[31] Kim, D. H.; Ringe, S.; Kim, H.; Kim, S.; Kim, B.; Bae, G.; Oh, H. S.; Jaouen, F.; Kim, W.; Kim, H. et al. Selective electrochemical reduction of nitric oxide to hydroxylamine by atomically dispersed iron catalyst. *Nat. Commun.* **2021**, *12*, 1856.

[32] Li, J. C.; Li, M.; An, N.; Zhang, S.; Song, Q. N.; Yang, Y. L.; Li, J.; Liu, X. Boosted ammonium production by single cobalt atom catalysts with high Faradic efficiencies. *Proc. Natl. Acad. Sci. USA* **2022**, *119*, e2123450119.

[33] Wu, Q.; Wang, H.; Shen, S. Y.; Huang, B. B.; Dai, Y.; Ma, Y. D. Efficient nitric oxide reduction to ammonia on a metal-free electrocatalyst. *J. Mater. Chem. A* **2021**, *9*, 5434–5441.

[34] Sa, Y. J.; Park, C.; Jeong, H. Y.; Park, S. H.; Lee, Z.; Kim, K. T.; Park, G. G.; Joo, S. H. Carbon nanotubes/heteroatom-doped carbon core-sheath nanostructures as highly active, metal-free oxygen reduction electrocatalysts for alkaline fuel cells. *Angew. Chem.* **2014**, *126*, 4186–4190.

[35] Choe, J.; Sun, W. T.; Ombrello, T.; Carter, C. Plasma assisted ammonia combustion: Simultaneous NO_x reduction and flame enhancement. *Combust. Flame* **2021**, *228*, 430–432.

[36] Ren, Z. B.; Zhang, H. N.; Wang, S. H.; Huang, B. B.; Dai, Y.; Wei, W. Nitric oxide reduction reaction for efficient ammonia synthesis on topological nodal-line semimetal Cu_2Si monolayer. *J. Mater. Chem. A* **2022**, *10*, 8568–8577.

[37] Chen, R.; Fang, X.; Li, Z.; Liu, Z. Selective catalytic reduction of NO_x with NH_3 over a novel MOF-derived MnO_x catalyst. *Appl. Catal. A: Gen.* **2022**, *643*, 118754.

[38] Tabassum, H.; Guo, W. H.; Meng, W.; Mahmood, A.; Zhao, R.; Wang, Q. F.; Zou, R. Q. Metal-organic frameworks derived cobalt phosphide architecture encapsulated into B/N Co-doped graphene nanotubes for all pH value electrochemical hydrogen evolution. *Adv. Energy Mater.* **2017**, *7*, 1601671.

[39] Cui, C. X.; Gao, Y.; Li, J.; Yang, C.; Liu, M.; Jin, H. L.; Xia, Z. H.; Dai, L. M.; Lei, Y.; Wang, J. C. et al. Origins of boosted charge storage on heteroatom-doped carbons. *Angew. Chem.* **2020**, *132*, 8002–8007.

[40] Yan, D. F.; Dou, S.; Tao, L.; Liu, Z. J.; Liu, Z. G.; Huo, J.; Wang, S. Y. Electropolymerized supermolecule derived N, P co-doped carbon nanofiber networks as a highly efficient metal-free electrocatalyst for the hydrogen evolution reaction. *J. Mater. Chem. A* **2016**, *4*, 13726–13730.

[41] Tabassum, H.; Zou, R. Q.; Mahmood, A.; Liang, Z. B.; Guo, S. J. A catalyst-free synthesis of B, N co-doped graphene nanostructures with tunable dimensions as highly efficient metal free dual electrocatalysts. *J. Mater. Chem. A* **2016**, *4*, 16469–16475.

[42] Chen, Z. P.; Mitchell, S.; Vorobyeva, E.; Leary, R. K.; Hauert, R.; Furnival, T.; Ramasse, Q. M.; Thomas, J. M.; Midgley, P. A.; Dontsova, D. et al. Stabilization of single metal atoms on graphitic carbon nitride. *Adv. Funct. Mater.* **2017**, *27*, 1605785.

[43] Zhang, X. F.; Yan, P. Q.; Xu, J. K.; Li, F.; Herold, F.; Etzold, B. J. M.; Wang, P.; Su, D. S.; Lin, S.; Qi, W. et al. Methanol conversion on borocarbonitride catalysts: Identification and quantification of active sites. *Sci. Adv.* **2020**, *6*, eaba5778.

[44] Wang, S. Y.; Iyyamperumal, E.; Roy, A.; Xue, Y. H.; Yu, D. S.; Dai, L. M. Vertically aligned BCN nanotubes as efficient metal-free electrocatalysts for the oxygen reduction reaction: A synergetic effect by co-doping with boron and nitrogen. *Angew. Chem., Int. Ed.* **2011**, *50*, 11756–11760.

[45] Wang, W. L.; Bai, X. D.; Liu, K. H.; Xu, Z.; Golberg, D.; Bando, Y.; Wang, E. G. Direct synthesis of B-C-N single-walled nanotubes by bias-assisted hot filament chemical vapor deposition. *J. Am. Chem. Soc.* **2006**, *128*, 6530–6531.

[46] Zheng, Y.; Jiao, Y.; Ge, L.; Jaroniec, M.; Qiao, S. Z. Two-step boron and nitrogen doping in graphene for enhanced synergistic catalysis. *Angew. Chem.* **2013**, *125*, 3192–3198.

[47] Shi, L.; Yin, Y.; Wang, S. B.; Sun, H. Q. Rational catalyst design for N_2 reduction under ambient conditions: Strategies toward enhanced conversion efficiency. *ACS Catal.* **2020**, *10*, 6870–6899.

[48] Tabassum, H.; Qu, C.; Cai, K. T.; Aftab, W.; Liang, Z. B.; Qiu, T. J.; Mahmood, A.; Meng, W.; Zou, R. Q. Large-scale fabrication of BCN nanotube architecture entangled on a three-dimensional carbon skeleton for energy storage. *J. Mater. Chem. A* **2018**, *6*, 21225–21230.

[49] Choi, C. H.; Park, S. H.; Woo, S. I. Binary and ternary doping of nitrogen, boron, and phosphorus into carbon for enhancing electrochemical oxygen reduction activity. *ACS Nano* **2012**, *6*, 7084–7091.

[50] Guo, F. S.; Yang, P. J.; Pan, Z. M.; Cao, X. N.; Xie, Z. L.; Wang, X. C. Carbon-doped BN nanosheets for the oxidative dehydrogenation of ethylbenzene. *Angew. Chem.* **2017**, *129*, 8343–8347.

[51] Légaré, M. A.; Bélanger-Chabot, G.; Dewhurst, R. D.; Welz, E.; Krummenacher, I.; Engels, B.; Braunschweig, H. Nitrogen fixation and reduction at boron. *Science* **2018**, *359*, 896–900.

[52] Yu, X. M.; Han, P.; Wei, Z. X.; Huang, L. S.; Gu, Z. X.; Peng, S. J.; Ma, J. M.; Zheng, G. F. Boron-doped graphene for electrocatalytic N_2 reduction. *Joule* **2018**, *2*, 1610–1622.

[53] Jiao, Y.; Zheng, Y.; Jaroniec, M.; Qiao, S. Z. Origin of the electrocatalytic oxygen reduction activity of graphene-based catalysts: A roadmap to achieve the best performance. *J. Am. Chem. Soc.* **2014**, *136*, 4394–4403.

[54] Panchakarla, L. S.; Subrahmanyam, K. S.; Saha, S. K.; Govindaraj, A.; Krishnamurthy, H. R.; Waghmare, U. V.; Rao, C. N. R. Synthesis, structure, and properties of boron-and nitrogen-doped graphene. *Adv. Mater.* **2009**, *21*, 4726–4730.

[55] Lu, Z. S.; Lv, P.; Yang, Z. X.; Li, S.; Ma, D. W.; Wu, R. Q. A promising single atom catalyst for CO oxidation: Ag on boron vacancies of h-BN sheets. *Phys. Chem. Chem. Phys.* **2017**, *19*, 16795–16805.

[56] Liu, Z. M.; Gao, D. Z.; Hu, L. N.; Liu, F.; Liu, H.; Li, Y.; Zhang, J.; Xue, Y. M.; Tang, C. C. Metal-free boron-rich borocarbonitride catalysts for high-efficient oxygen reduction to produce hydrogen peroxide. *ChemistrySelect* **2022**, *7*, e202104203.

[57] Feng, Y.; Yao, J. F. Design of melamine sponge-based three-dimensional porous materials toward applications. *Ind. Eng. Chem. Res.* **2018**, *57*, 7322–7330.

[58] Chen, X.; Liu, Y.; Ke, X. X.; Weerasooriya, R.; Li, H.; Wang, L. C.; Wu, Y. C. A green method to synthesize AuNPs/mpg-C_3N_4 nanocomposites for constructing anti-interference electrochemical sensing interface toward methylmercury. *J. Alloys Compd.* **2021**,

853, 157365.
[59] B. V.; Usachov, D. Y.; Fedorov, A. V.; Marangoni, T.; Haberer, D.; Tresca, C.; Profeta, G.; Caciuc, V.; Tsukamoto, S.; Atodiresei, N. et al. Boron-doped graphene nanoribbons: Electronic structure and Raman fingerprint. *ACS Nano* **2018**, *12*, 7571–7582.
[60] Shi, M. M.; Bao, D.; Wulan, B. R.; Li, Y. H.; Zhang, Y. F.; Yan, J. M.; Jiang, Q. Au sub-nanoclusters on TiO_2 toward highly efficient and selective electrocatalyst for N_2 conversion to NH_3 at ambient conditions. *Adv. Mater.* **2017**, *29*, 1606550.
[61] He, H. M.; Zhu, Q. Q.; Yan, Y.; Zhang, H. W.; Han, Z. Y.; Sun, H. M.; Chen, J.; Li, C. P.; Zhang, Z. H.; Du, M. Metal-organic framework supported Au nanoparticles with organosilicone coating for high-efficiency electrocatalytic N_2 reduction to NH_3. *Appl. Catal. B:Environ.* **2022**, *302*, 120840.
[62] Zhao, X.; Yang, Z. Q.; Kuklin, A. V.; Baryshnikov, G. V.; Ågren, H.; Zhou, X. H.; Zhang, H. B. Efficient ambient electrocatalytic ammonia synthesis by nanogold triggered via boron clusters combined with carbon nanotubes. *ACS Appl. Mater. Interfaces* **2020**, *12*, 42821–42831.
[63] Li, W. Y.; Zhang, C.; Han, M. M.; Ye, Y. X.; Zhang, S. B.; Liu, Y. Y.; Wang, G. Z.; Liang, C. H.; Zhang, H. M. Ambient electrosynthesis of ammonia using core-shell structured Au@C catalyst fabricated by one-step laser ablation technique. *ACS Appl. Mater. Interfaces* **2019**, *11*, 44186–44195.
[64] Deshpande, S.; Greeley, J. First-principles analysis of coverage, ensemble, and solvation effects on selectivity trends in NO electroreduction on Pt_3Sn alloys. *ACS Catal.* **2020**, *10*, 9320–9327.
[65] Niu, H.; Zhang, Z. F.; Wang, X. T.; Wan, X. H.; Kuai, C. G.; Guo, Y. Z. A feasible strategy for identifying single-atom catalysts toward electrochemical NO-to-NH_3 conversion. *Small* **2021**, *17*, 2102396.
[66] Xiong, Y. H.; Li, Y. T.; Wan, S. P.; Yu, Y.; Zhang, S. L.; Zhong, Q. Ferrous-based electrolyte for simultaneous NO absorption and electroreduction to NH_3 using Au/rGO electrode. *J. Hazard. Mater.* **2022**, *430*, 128451.
[67] Liang, J.; Liu, Q.; Alshehri, A. A.; Sun, X. P. Recent advances in nanostructured heterogeneous catalysts for N-cycle electrocatalysis. *Nano Res. Energy* **2022**, *1*, e9120010.
[68] Choi, J.; Du, H. L.; Nguyen, C. K.; Suryanto, B. H. R.; Simonov, A. N.; MacFarlane, D. R. Electroreduction of nitrates, nitrites, and gaseous nitrogen oxides: A potential source of ammonia in dinitrogen reduction studies. *ACS Energy Lett.* **2020**, *5*, 2095–2097.
[69] de Vooys, A. C. A.; Koper, M. T. M.; van Santen, R. A.; van Veen, J. A. R. Mechanistic study on the electrocatalytic reduction of nitric oxide on transition-metal electrodes. *J. Catal.* **2001**, *202*, 387–394.
[70] Qin, Q.; Heil, T.; Antonietti, M.; Oschatz, M. Single-site gold catalysts on hierarchical N-doped porous noble carbon for enhanced electrochemical reduction of nitrogen. *Small Methods* **2018**, *2*, 1800202.
[71] Xue, Z. H.; Zhang, S. N.; Lin, Y. X.; Su, H.; Zhai, G. Y.; Han, J. T.; Yu, Q. Y.; Li, X. H.; Antonietti, M.; Chen, J. S. Electrochemical reduction of N_2 into NH_3 by donor-acceptor couples of Ni and Au nanoparticles with a 67.8% Faradaic efficiency. *J. Am. Chem. Soc.* **2019**, *141*, 14976–14980.
[72] Hu, Q.; Gao, K. R.; Wang, X. D.; Zheng, H. J.; Cao, J. Y.; Mi, L. R.; Huo, Q. H.; Yang, H. P.; Liu, J. H.; He, C. X. Subnanometric Ru clusters with upshifted D band center improve performance for alkaline hydrogen evolution reaction. *Nat. Commun.* **2022**, *13*, 3958.
[73] Liang, X.; Fu, N. H.; Yao, S. C.; Li, Z.; Li, Y. D. The progress and outlook of metal single-atom-site catalysis. *J. Am. Chem. Soc.* **2022**, *144*, 18155–18174.
[74] Liu, S. F.; Xu, W.; Niu, Y. M.; Zhang, B. S.; Zheng, L. R.; Liu, W.; Li, L.; Wang, J. H. Ultrastable Au nanoparticles on Titania through an encapsulation strategy under oxidative atmosphere. *Nat. Commun.* **2019**, *10*, 5790.
[75] Jin, H. Y.; Wang, J.; Su, D. F.; Wei, Z. Z.; Pang, Z. F.; Wang, Y. *In situ* cobalt-cobalt oxide/N-doped carbon hybrids as superior bifunctional electrocatalysts for hydrogen and oxygen evolution. *J. Am. Chem. Soc.* **2015**, *137*, 2688–2694.
[76] Zhang, H.; Zhou, Y.; Li, C. G.; Chen, S. L.; Liu, L.; Liu, S. W.; Yao, H. M.; Hou, H. Q. Porous nitrogen doped carbon foam with excellent resilience for self-supported oxygen reduction catalyst. *Carbon* **2015**, *95*, 388–395.
[77] Chen, J. Z.; Xu, J. L.; Zhou, S.; Zhao, N.; Wong, C. P. Nitrogen-doped hierarchically porous carbon foam: A free-standing electrode and mechanical support for high-performance supercapacitors. *Nano Energy* **2016**, *25*, 193–202.
[78] Chen, L.; Du, R.; Zhu, J. H.; Mao, Y. Y.; Xue, C.; Zhang, N.; Hou, Y. L.; Zhang, J.; Yi, T. Three-dimensional nitrogen-doped graphene nanoribbons aerogel as a highly efficient catalyst for the oxygen reduction reaction. *Small* **2015**, *11*, 1423–1429.
[79] Pang, Y. Y.; Wang, K.; Xie, H.; Sun, Y.; Titirici, M. M.; Chai, G. L. Mesoporous carbon hollow spheres as efficient electrocatalysts for oxygen reduction to hydrogen peroxide in neutral electrolytes. *ACS Catal.* **2020**, *10*, 7434–7442.
[80] Chen, S. C.; Chen, Z. H.; Siahrostami, S.; Kim, T. R.; Nordlund, D.; Sokaras, D.; Nowak, S.; To, J. W.; Higgins, D.; Sinclair, R. et al. Defective carbon-based materials for the electrochemical synthesis of hydrogen peroxide. *ACS Sustain. Chem. Eng.* **2018**, *6*, 311–317.
[81] Yin, H. B.; Chen, Z.; Xiong, S. C.; Chen, J. J.; Wang, C. Z.; Wang, R.; Kuwahara, Y.; Luo, J. S.; Yamashita, H.; Peng, Y. et al. Alloying effect-induced electron polarization drives nitrate electroreduction to ammonia. *Chem Catal.* **2021**, *1*, 1088–1103.
[82] Zhang, L. C.; Zhou, Q.; Liang, J.; Yue, L. C.; Li, T. S.; Luo, Y. S.; Liu, Q.; Li, N.; Tang, B.; Gong, F. et al. Enhancing electrocatalytic NO reduction to NH_3 by the CoS nanosheet with sulfur vacancies. *Inorg. Chem.* **2022**, *61*, 8096–8102.
[83] Frear, D. S.; Burrell, R. C. Spectrophotometric method for determining hydroxylamine reductase activity in higher plants. *Anal. Chem.* **1955**, *27*, 1664–1665.
[84] Ye, S. H.; Luo, F. Y.; Xu, T. T.; Zhang, P. Y.; Shi, H. D.; Qin, S. Q.; Wu, J. P.; He, C. X.; Ouyang, X. P.; Zhang, Q. L. et al. Boosting the alkaline hydrogen evolution of Ru nanoclusters anchored on B/N-doped graphene by accelerating water dissociation. *Nano Energy* **2020**, *68*, 104301.
[85] Mannan, A.; Hirano, Y.; Quitain, A. T.; Koinuma, M.; Kida, T. Graphene oxide to B, N co-doped graphene through tris-dimethylaminoborane complex by hydrothermal implantation. *Am. J. Mater. Sci.* **2019**, *9*, 22–28.
[86] Fedoseeva, Y. V.; Lobiak, E. V.; Shlyakhova, E. V.; Kovalenko, K. A.; Kuznetsova, V. R.; Vorfolomeeva, A. A.; Grebenkina, M. A.; Nishchakova, A. D.; Makarova, A. A.; Bulusheva, L. G. et al. Hydrothermal activation of porous nitrogen-doped carbon materials for electrochemical capacitors and sodium-ion batteries. *Nanomaterials* **2020**, *10*, 2163.
[87] Domnich, V.; Reynaud, S.; Haber, R. A.; Chhowalla, M. Boron carbide: Structure, properties, and stability under stress. *J. Am Ceram Soc.* **2011**, *94*, 3605–3628.
[88] Chakrabarty, K.; Chen, W. C.; Baker, P. A.; Vijayan, V. M.; Chen, C. C.; Catledge, S. A. Superhard boron-rich boron carbide with controlled degree of crystallinity. *Materials* **2020**, *13*, 3622.
[89] Werheit, H.; Au, T.; Schmechel, R.; Shalamberidze, S. O.; Kalandadze, G. I.; Eristavi, A. M. IR-active phonons and structure elements of isotope-enriched boron carbide. *J. Solid State Chem.* **2000**, *154*, 79–86.
[90] He, Y. H.; Guo, H.; Hwang, S.; Yang, X. X.; He, Z. Z.; Braaten, J.; Karakalos, S.; Shan, W. T.; Wang, M. Y.; Zhou, H. et al. Single cobalt sites dispersed in hierarchically porous nanofiber networks for durable and high-power PGM-free cathodes in fuel cells. *Adv. Mater.* **2020**, *32*, 2003577.
[91] Lin, W. W.; Chen, H.; Lin, G. B.; Yao, S. Y.; Zhang, Z. H.; Qi, J. Z.; Jing, M. Z.; Song, W. Y.; Li, J.; Liu, X. et al. Creating frustrated lewis pairs in defective boron carbon nitride for electrocatalytic nitrogen reduction to ammonia. *Angew. Chem., Int. Ed.* **2022**, *61*, e202207807.
[92] Zhang, J. S.; Zhang, M. W.; Sun, R. Q.; Wang, X. C. A facile band alignment of polymeric carbon nitride semiconductors to construct isotype heterojunctions. *Angew. Chem.* **2012**, *124*, 10292–10296.
[93] Yang, Y. T.; Wang, Y.; Wang, X.; Chen, S. Q.; Duan, L. M.; Zhang, W.; Li, W. F.; Liu, J. H. Tailoring electron-riched boron sites in BCN for nitrogen fixation via alternate mechanism. *Adv.*

Mater. Interfaces **2022**, *9*, 2101842.
[94] Huang, C. J.; Chen, C.; Zhang, M. W.; Lin, L. H.; Ye, X. X.; Lin, S.; Antonietti, M.; Wang, X. C. Carbon-doped BN nanosheets for metal-free photoredox catalysis. *Nat. Commun.* **2015**, *6*, 7698.
[95] Tabbal, M.; Christidis, T.; Isber, S.; Mérel, P.; El Khakani, M. A.; Chaker, M.; Amassian, A.; Martinu, L. Correlation between the sp^2-phase nanostructure and the physical properties of unhydrogenated carbon nitride. *J. Appl. Phys.* **2005**, *98*, 044310.
[96] Zhang, J. S.; Zhang, G. G.; Chen, X. F.; Lin, S.; Möhlmann, L.; Dołęga, G., Lipner, G.; Antonietti, M.; Blechert, S.; Wang, X. C. Co-monomer control of carbon nitride semiconductors to optimize hydrogen evolution with visible light. *Angew. Chem., Int. Ed.* **2012**, *51*, 3183–3187.
[97] Zhao, J.; Lin, B. N.; Zhu, Y. F.; Zhou, Y. H.; Liu, H. Y. Phosphor-doped hexagonal boron nitride nanosheets as effective acid-base bifunctional catalysts for one-pot deacetalization-Knoevenagel cascade reactions. *Catal. Sci. Technol.* **2018**, *8*, 5900–5905.
[98] Zhang, S.; Zhao, Y. X.; Shi, R.; Waterhouse, G. I. N.; Zhang, T. R. Photocatalytic ammonia synthesis: Recent progress and future. *EnergyChem* **2019**, *1*, 100013.
[99] Nakata, K.; Ozaki, T.; Terashima, C.; Fujishima, A.; Einaga, Y. High-yield electrochemical production of formaldehyde from CO_2 and seawater. *Angew. Chem., Int. Ed.* **2014**, *53*, 871–874.
[100] Stephan, D. W.; Erker, G. Frustrated Lewis pairs: Metal-free hydrogen activation and more. *Angew. Chem., Int. Ed.* **2010**, *49*, 46–76.
[101] Stephan, D. W.; Erker, G. Frustrated Lewis pair chemistry of carbon, nitrogen and sulfur oxides. *Chem. Sci.* **2014**, *5*, 2625–2641.
[102] Mömming, C. M.; Otten, E.; Kehr, G.; Fröhlich, R.; Grimme, S.; Stephan, D. W.; Erker, G. Reversible metal-free carbon dioxide binding by frustrated Lewis pairs. *Angew. Chem., Int. Ed.* **2009**, *48*, 6643–6646.
[103] Woińska1, M.; Milowska, K. Z.; Majewski, J. A. Electronic structure of graphene functionalized with boron and nitrogen. *Phys. Status Solidi (C)* **2013**, *10*, 1167–1171.
[104] Shi, P. H.; Su, R. J.; Wan, F. Z.; Zhu, M. C.; Li, D. X.; Xu, S. H. Co_3O_4 nanocrystals on graphene oxide as a synergistic catalyst for degradation of Orange II in water by advanced oxidation technology based on sulfate radicals. *Appl. Catal. B: Environ.* **2012**, *123–124*, 265–272.
[105] Jeong, H. M.; Lee, J. W.; Shin, W. H.; Choi, Y. J.; Shin, H. J.; Kang, J. K.; Choi, J. W. Nitrogen-doped graphene for high-performance ultracapacitors and the importance of nitrogen-doped sites at basal planes. *Nano Lett.* **2011**, *11*, 2472–2477.
[106] Wang, Y.; Shao, Y. Y.; Matson, D. W.; Li, J. H.; Lin, Y. H. Nitrogen-doped graphene and its application in electrochemical biosensing. *ACS Nano* **2010**, *4*, 1790–1798.
[107] Bepete, G.; Voiry, D.; Chhowalla, M.; Chiguvare, Z.; Coville, N. J. Incorporation of small BN domains in graphene during CVD using methane, boric acid and nitrogen gas. *Nanoscale* **2013**, *5*, 6552–6557.
[108] Chen, X.; Qiao, Q. A.; An, L.; Xia, D. G. Why do boron and nitrogen doped α-and γ-graphyne exhibit different oxygen reduction mechanism? A first-principles study. *J. Phys. Chem. C* **2015**, *119*, 11493–11498.
[109] Q.; Su, J. C.; Chen, H. L.; Wang, D. Q.; Tian, X. Y.; Zhang, Y. J.; Feng, X.; Wang, S.; Li, J.; Jin, H. L. Highly conductive nitrogen-doped sp^2/sp^3 hybrid carbon as a conductor-free charge storage host. *Adv. Funct. Mater.* **2022**, *32*, 2209201.
[110] Steiner, U. B.; Caseri, W. R.; Suter, U. W.; Rehahn, M.; Schmitz, L. Ultrathin layers of low-and high-molecular-weight imides on gold and copper. *Langmuir* **1993**, *9*, 3245–3254.
[111] Zeng, L.; Dai, C. H.; Liu, B.; Xue, C. Oxygen-assisted stabilization of single-atom Au during photocatalytic hydrogen evolution. *J. Mater. Chem. A* **2019**, *7*, 24217–24221.
[112] Duan, X. P.; Tian, X. L.; Ke, J. H.; Yin, Y.; Zheng, J. W.; Chen, J.; Cao, Z. M.; Xie, Z. X.; Yuan, Y. Z. Size controllable redispersion of sintered Au nanoparticles by using iodohydrocarbon and its implications. *Chem. Sci.* **2016**, *7*, 3181–3187.
[113] Kim, D.; Shin, D.; Heo, J.; Lim, H.; Lim, J. A.; Jeong, H. M.; Kim, B. S.; Heo, I.; Oh, I.; Lee, B. et al. Unveiling electrode-electrolyte design-based NO reduction for NH_3 synthesis. *ACS Energy Lett.* **2020**, *5*, 3647–3656.
[114] Zhou, Q.; Gong, F.; Xie, Y. L.; Xia, D. W.; Hu, Z. G.; Wang, S. J.; Liu, L. S.; Xiao, R. A general strategy for designing metal-free catalysts for highly-efficient nitric oxide reduction to ammonia. *Fuel* **2022**, *310*, 122442.
[115] Luo, Y. J.; Chen, K.; Shen, P.; Li, X. C.; Li, X. T.; Li, Y. H.; Chu, K. B-doped MoS_2 for nitrate electroreduction to ammonia. *J. Colloid Interf. Sci.* **2023**, *629*, 950–957.
[116] Yang, C. H.; Zhu, Y. T.; Liu, J. Q.; Qin, Y. C.; Wang, H. Q.; Liu, H. L.; Chen, Y. N.; Zhang, Z. C.; Hu, W. P. Defect engineering for electrochemical nitrogen reduction reaction to ammonia. *Nano Energy* **2020**, *77*, 105126.
[117] Ouyang, W. C.; Zhi, Q. M.; Gong, L. L.; Sun, H.; Liu, M. H.; Zhang, J.; Han, X.; Xia, Z. H.; Zhang, L. P. Rational design of boron-containing co-doped graphene as highly efficient electro-catalysts for the nitrogen reduction reaction. *J. Mater. Chem. A* **2021**, *9*, 24590–24599.
[118] Jiao, J. Q.; Wei, Y. C.; Zhao, Z.; Zhong, W. J.; Liu, J.; Li, J. M.; Duan, A. J.; Jiang, G. Y. Synthesis of 3D ordered macroporous TiO_2-supported Au nanoparticle photocatalysts and their photocatalytic performances for the reduction of CO_2 to methane. *Catal. Today* **2015**, *258*, 319–326.
[119] Margitfalvi, J. L.; Fási, A.; Hegedűs, M.; Lónyi, F.; Gőbölös, S.; Bogdanchikova, N. Au/MgO catalysts modified with ascorbic acid for low temperature CO oxidation. *Catal. Today* **2002**, *72*, 157–169.
[120] Veith, G. M.; Lupini, A. R.; Pennycook, S. J.; Ownby, G. W.; Dudney, N. J. Nanoparticles of gold on γ-Al_2O_3 produced by dc magnetron sputtering. *J. Catal.* **2005**, *231*, 151–158.
[121] Zhao, L. Y.; Levendorf, M.; Goncher, S.; Schiros, T.; Pálová, L.; Zabet-Khosousi, A.; Rim, K. T.; Gutiérrez, C.; Nordlund, D.; Jaye, C. et al. Local atomic and electronic structure of boron chemical doping in monolayer graphene. *Nano Lett.* **2013**, *13*, 4659–4665.
[122] Ferrighi, L.; Trioni, M. I.; Di Valentin, C. Boron-doped, nitrogen-doped, and codoped graphene on Cu (111): A DFT + vdW study. *J. Phys. Chem. C* **2015**, *119*, 6056–6064.
[123] Matkovich, V. I. *Boron and Refractory Borides*; Springer: Berlin, Heidelberg, 1977; pp 1–656.
[124] D. Y.; Jeon, W.; Tu, N. D. K.; Yeo, S. Y.; Lee, S. S.; Sung, B. J.; Chang, H.; Lim, J. A.; Kim, H. High-concentration boron doping of graphene nanoplatelets by simple thermal annealing and their supercapacitive properties. *Sci. Rep.* **2015**, *5*, 9817.
[125] Wen, G. L.; Zhao, W.; Chen, X.; Liu, J. Q.; Wang, Y.; Zhang, Y.; Huang, Z. J.; Wu, Y. C. N-doped reduced graphene oxide/MnO_2 nanocomposite for electrochemical detection of Hg^{2+} by square wave stripping voltammetry. *Electrochim. Acta* **2018**, *291*, 95–102.
[126] Zhao, Q.; Wu, W. X.; Wei, X. Y.; Jiang, S. L.; Zhou, T.; Li, Q.; Lu, Q. Graphitic carbon nitride as electrode sensing material for tetrabromobisphenol-A determination. *Sensors Actuat. B: Chem.* **2017**, *248*, 673–681.
[127] Kong, Y.; Li, Y.; Yang, B.; Li, Z. J.; Yao, Y.; Lu, J. G.; Lei, L. C.; Wen, Z. H.; Shao, M. H.; Hou, Y. Boron and nitrogen co-doped porous carbon nanofibers as metal-free electrocatalysts for highly efficient ammonia electrosynthesis. *J. Mater. Chem. A* **2019**, *7*, 26272–26278.
[128] Wan, H.; Bagger, A.; Rossmeisl, J. Electrochemical nitric oxide reduction on metal surfaces. *Angew. Chem.* **2021**, *133*, 22137–22143.
[129] Dong, W. F.; Zhang, N.; Li, S. X.; Min, S. X.; Peng, J.; Liu, W. Y.; Zhan, D. P.; Bai, H. C. A Mn single atom catalyst with Mn-N_2O_2 sites integrated into carbon nanosheets for efficient electrocatalytic CO_2 reduction. *J. Mater. Chem. A* **2022**, *10*, 10892–10901.
[130] Yuan, M. L.; Zhang, H. H.; Xu, Y.; Liu, R. J.; Wang, R.; Zhao, T. K.; Zhang, J. X.; Liu, Z. J.; He, H. Y.; Yang, C. et al. Artificial frustrated Lewis pairs facilitating the electrochemical N_2 and CO_2 conversion to urea. *Chem Catal.* **2022**, *2*, 309–320.